Wave-induced coherent turbulence structures and sediment resuspension in the nearshore of a prototype-scale sandy barrier beach

Hachem Kassem, Charlotte E.L. Thompson, Carl L. Amos, Ian H. Townend

www.elsevier.com/locate/csr

PII: S0278-4343(15)30062-5
DOI: http://dx.doi.org/10.1016/j.csr.2015.09.007
Reference: CSR3276

To appear in: *Continental Shelf Research*

Received date: 15 May 2015
Accepted date: 10 September 2015

Cite this article as: Hachem Kassem, Charlotte E.L. Thompson, Carl L. Amo and Ian H. Townend, Wave-induced coherent turbulence structures and sedimen resuspension in the nearshore of a prototype-scale sandy barrier beach *Continental Shelf Research,* http://dx.doi.org/10.1016/j.csr.2015.09.007

Title: Wave-induced coherent turbulence structures and sediment resuspension in the nearshore of a prototype-scale sandy barrier beach

Authors:

Kassem, Hachem [a]

Thompson, Charlotte E.L. [a]

Amos, Carl L. [a]

Townend, Ian H. [a]

Affiliations:

[a] Ocean and Earth Science, National Oceanography Centre Southampton, University of Southampton Waterfront Campus, European Way, Southampton SO14 3ZH, United Kingdom

Corresponding author email: Hachem.kassem@soton.ac.uk m: 00447557356965

Thompson, Charlotte E.L. : celt1@noc.soton.ac.uk

Amos, Carl L.: cla8@noc.soton.ac.uk

Townend, Ian H.: I.Townend@soton.ac.uk

Abstract:

The suspension of sediments by oscillatory flows is a complex case of fluid–particle interaction. The aim of this study is to provide insight into the spatial (time) and scale (frequency) relationships between wave-generated boundary layer turbulence and event-driven sediment transport beneath irregular shoaling and breaking waves in the nearshore of a prototype sandy barrier beach, using data collected through the Barrier Dynamics Experiment II (BARDEX II). Statistical, quadrant and spectral analyses reveal the anisotropic and intermittent nature of Reynolds' stresses (momentum exchange) in the wave boundary layer, in all three orthogonal planes of motion. The fractional contribution of coherent turbulence structures appears to be dictated by the structural form of eddies beneath plunging and spilling breakers, which in turn define the net sediment mobilisation towards or away from the barrier, and hence ensuing erosion and accretion trends. A standing transverse wave is also observed in the flume, contributing to the substantial skewness of spanwise turbulence. Observed low frequency suspensions are closely linked to the mean flow (wave) properties. Wavelet analysis reveals that the entrainment and maintenance of sediment in suspension through a cluster of bursting sequence is associated with the passage of intermittent slowly–evolving large structures, which can modulate the frequency of smaller motions. Outside the boundary layer, small scale, higher frequency turbulence drives the suspension. The extent to which these spatially varied perturbation clusters persist is associated with suspension events in the high frequency scales, decaying as the turbulent motion ceases to supply momentum, with an observed hysteresis effect.

Highlights

Slowly evolving coherent turbulence clusters induce cumulative suspension events

Spatial and temporal scales of resuspension and coherent structures are interdependent

Flume geometry amplifies turbulence anisotropy through standing transverse wave

Keywords

Coherent turbulence structures, sediment resuspension, wavelets

1.0 Introduction

The suspension of sediment in turbulent flows is a complex case of fluid-particle interaction, governed by shear stresses (momentum exchanges) at the bed and within the benthic boundary layer (BBL). Defining the physical processes which dictate the resuspension of sediments in coastal and estuarine settings is fundamental for accurate predictions of bed morphology evolution (Van Rijn et al., 2007), and has profound implications for the biogeochemical processes that shape their local ecology (Thompson et al., 2011). It is also a prerequisite to quantifying erosion and deposition trends, and hence guiding engineering applications such as beach nourishment, defence schemes against erosion and flooding, maintenance of marine infrastructure and waterways, and aggregate dredging. There is a genuine need for better, robust models of suspended sediment transport in the coastal zone (Aagaard and Jensen, 2013). In a vision paper on future research needs in coastal dynamics, Van Rijn et al. (2013) highlighted the pressing need for research to support such models, focusing in particular on sand transport in the shoreface (non–breaking waves), surf and swash zones; employing field and controlled laboratory experiments.

The mobilisation of sediments in the nearshore and shoreface is dominated by wave-induced bed shear stresses in moderate and stormy conditions (Thompson et al., 2012). The vertical structure of sediment flux components on the shoreface and in the inner surf zone, as well as the dynamics of sediment transport under shoaling waves in the nearshore, are both considered to be insufficiently understood (Van Rijn et al., 2013). This requires prioritising research with reference to coherent flow structures and the intermittent stirring of sediments by breaking and shoaling waves, and the time-history effects of suspended sediments under irregular wave conditions [ibid.]. Understanding the spatial, temporal, and frequency characteristics of sediment suspension events in relation to turbulent fluctuations, both in structural form and in temporal distribution, is an important step towards providing a more satisfactory conceptual model for describing suspended sediment transport.

The role played by bed–generated coherent eddy structures in entraining and transporting sediment particles is widely acknowledged, yet the exact mechanism is still unclear (Dey et al., 2012; Ji et al., 2013). Coherent turbulence structures have been defined, albeit reluctantly, as “connected turbulent fluid masses with instantaneously phase-correlated vorticity over their spatial extent” (1986; Hussain, 1983). Fiedler (1988) added several criteria to the definition, namely; composite scales, recurrent patterns (lifespan longer than the passage time of the structure), high organisation and quasi-periodic appearance. Besides the “conventional” bursting events which describe the intermittent, energetic process resulting from the passage of near-wall vortices as perceived by passive markers

and/or visualisation studies (Schoppa and Hussain, 2002); one may identify vortices induced by wave breaking (Aagaard and Hughes, 2010), or by flow separation from vortex ripples upon reversal in an oscillatory flow, i.e. vortex entrainment/shedding (Amoudry et al., 2013). Vortex shedding from bedforms in wave dominated flows was first reported by Bagnold and Taylor (1946). As flow reverses over steep two-dimensional bedforms, the benthic boundary layer can separate from the bed, trapping sediments and ejecting them higher into the flow (O'hara Murray et al., 2011). This is in essence a repeatable and hence coherent convective entrainment process (Nielsen, 1992) that is observed in both regular (at half cycle) and irregular wave conditions (O'hara Murray et al., 2012; O'hara Murray et al., 2011; Thorne et al., 2003). Where vortex pairs may develop, sediments may be violently ejected much higher (several orders of a ripple height) than classically described (Williams et al., 2007).

The intermittent transfer of momentum by coherent structures of turbulence is manifest by velocity fluctuations, and is linked to short-term variations in near-bed stresses (Heathershaw, 1974; Laufer, 1975). This is evident in the turbulent “bursting” process (Kline et al., 1967; Offen and Kline, 1974, 1975), which is a critical mechanism for production of turbulent kinetic energy (Dey et al., 2012; Schoppa and Hussain, 2002). Turbulent bursting may be explained by the advection of spatially distributed vortices and structural features past a fixed point of measurement (Robinson, 1991), although this may not detect how such vortices evolve in time (Schoppa and Hussain, 2002). The largest contributions to stress often occur through ejecting or sweeping motions (Soulsby, 1983). Typically, ejections are associated with entrainment of mass (sediment particles) into suspension, while sweeps are effective at transporting bedload (Cao, 1997; Dyer and Soulsby, 1988; Heathershaw, 1979; Keylock, 2007; Soulsby, 1983; Yuan et al., 2009). While ejections and sweeps reportedly occur in relatively equal proportions near the bed, the former type dominates higher in the water column (Cellino and Lemmin, 2004). Suspension of sediments is often related to large scale turbulence structures associated with clusters of ejections (Bennett et al., 1998; Kawanisi and Yokosi, 1993).

Recent sediment suspension models attempt to account for turbulent bursting by implementing entrainment functions that theoretically account for the average time and space scales of these motions (e.g. Cao (1997), Wu and Yang (2004), Wu and Jiang (2007)). Considerable recent work therefore focusses on the structural form of these features of flow, their role in fluid and sediment entrainment, bed shear stress generation, energy transfer and velocity asymmetry; and the influence of the space-time structure of the flow, with emphasis on oscillatory flows, and different bed roughnesses (Adrian and Marusic, 2012; Carstensen et al., 2010; Carstensen et al. (2012); Grigoriadis et al., 2013;

Hardy et al., 2010; Hare et al., 2014; Okamoto et al., 2007). Advanced visualisation and data analysis techniques reveal complex interactions between passing coherent energetic structures and sediments in suspension, such as particle response to turbulent fluctuations in the frequency domain (e.g. Liu et al., 2012), and modifications of the mean velocity profile by the dispersed sediments (e.g. Ji et al., 2013). The aim of this study is to describe the temporal and scale relationships between wave–generated boundary layer turbulence and event–driven sediment suspension in oscillatory flow in the nearshore of a prototype sandy barrier beach. In particular, two aspects are investigated: (a) the time–frequency characteristics that describe the relationship between turbulent burst cycles and ensuing sediment suspension; and (b) the scale of covariance of near–bed sediment resuspension events with wave–induced turbulent coherent structures as manifest by the intermittent Reynolds' Stresses.

2.0 Methodology

2.1 Experimental setup and wave conditions

The results presented here arise from the analysis of two wave data sets collected within the European HYDRALAB IV Barrier Dynamics Experiment II (BARDEX II) carried out at the Delta Flume facility/Deltares, the Netherlands, between June and July 2012 (Masselink et al., 2013). A barrier beach, 75 m wide (cross–shore), 5 m alongshore, was constructed from moderately sorted, medium fluvial sand with a median grain diameter, D_{50}, of 0.42mm. The barrier, backed by a lagoon and fronted by a 20 m flat section (of same bed material, 0.5 m deep), was subjected to a JONSWAP spectrum of waves, generated by a single-stroke wave paddle fitted with an automated reflection compensator to supress reflection and low frequency resonance, situated 49 m before the start of the 1:15 m seaward slope.

As part of these experiments, time–synched acoustic measurements of turbulence, suspension, and bed morphology were recorded from an instrumented frame at the nearshore position, situated just at the break of the seaward slope of the barrier (49 m from wave paddle). A schematic sketch of the frame and the barrier design is given in Figure 1. Turbulence data were collected by means of two coupled, downward-looking Nortek Vectrino Acoustic Doppler Velocimeters (ADVs) with a vertical offset of 26 cm and an across–flume horizontal offset of 36 cm, sampling at 25 Hz. Sediment suspensions were inferred from backscatter measured with an Aquatec Aquascat Acoustic Backscatter Profiling Sensor (ABS), with 1, 2, and 4 MHz channels, measuring between 5 and 95 cm below the instrument in 0.5 mm bins at 64 Hz (Thompson et al., 2013). Unfortunately, it was not possible to calibrate the ABS measurements (and hence infer volume/mass concentrations) due to failure of pump equipment. Subsequently, concentrations and backscatter are used

interchangeably in this work. Three dimensional bed morphology was inferred from a combination of a Marine Electronics 1.1 MHz dual sand ripple profiling system (SPRS) recording sequential cross–shore profiles and a 500 kHz Sector Scanning Sonar (SSS) which provided a 360◦ plan–view of the bedforms. Surface water elevation (pressure) was recorded through a 5 Hz self-logging Paraoscientific 745 pressure transducer, mounted 0.35 m above the bed. Although turbulence and bedform data were recorded for the entire length of each wave run, memory limitations in the ABS instrument mean bursts of a maximum length of 8 minutes are presented. As such, where turbulence records are analysed in conjunction with suspension data, these are trimmed accordingly.

2.2 Data collection, quality and pre-processing

The 3D instantaneous flow velocity field $(\mathrm{U}, \mathrm{V}, \mathrm{W})$ representing the streamwise (along-flume), cross–wise (across-flume); and vertical components of instantaneous velocity, respectively; is given by ADVs measuring at two discrete 7mm sample volumes above the bed (Figure 1c). However, ADVs are inherently contaminated by noise due to Doppler signal aliasing, bubbles, etc. (Mori et al., 2007) and inferred stresses are susceptible to errors due to sensor misalignment (Soulsby and Humphery, 1990). For quality control purposes, a threshold of measurement correlation based on the instrument sampling frequency was used (after Elgar et al. (2005)), giving ~70% as the lower limit. A limit of 20% corrupted data per record was subsequently applied, delimiting sequences where samples fall continuously below the accepted correlation threshold for > two seconds (Elgar et al., 2001; Feddersen, 2010). The records were then patched by applying a moving average algorithm interpolating the missing data, following Thompson et al. (2012). Subsequently, an axis–rotation algorithm is used to eliminate effects of sensor misalignment, following Elgar et al. (2001). A similar operation is applied to the y–z plane before the mean values of the rotated coordinates are deducted to remove the contamination of the “U” data by the “V” data.

To extract the turbulence component (u'), the mean flow velocity of each component $(\bar{\mathrm{u}})$, determined by applying a moving average as a low pass filter, is subtracted from the instantaneous flow field (u), before the record is zero–meaned and de–trended (Thompson et al., 2012). The numerator coefficients defining the filter window were selected by trial and error, with autocorrelation and cross–correlation tests applied for validation. It follows that two fluctuating components are identified, a wave-induced (periodic) component (denoted by $\mathrm{u}'_{\mathrm{wave}}$) and the residual “random/high frequency” component, u'. The signals are then de-spiked using the modified “true” 3 D phase space method by (Goring and Nikora, 2002, 2003) as modified by (Mori et al., 2007). It is to be noted that similar power (variance)

properties and scales in the time-frequency domain were observed before and after despiking, albeit with smaller magnitude stresses.

The non-directional wave parameters (peak wave periods and significant wave heights) were computed by zero-crossing and spectral analysis of the pressure variations, having compensated for transducer height above bed, and pressure attenuation with depth following Tucker and Pitt (2001). Bed morphology was inferred from the backscatter intensity of the SSS and SRPS records. Bed location was determined using the built-in 'bed detection' function of the SRPS dual-head programmer software (Marine Electronics Ltd.) with a threshold value (20 dB) above the average backscatter intensity, having adjusted for sound attenuation. Bed level data were then detrended to remove the bed slope, and de-spiked to remove outliers pertaining to high concentration suspension events. A zero-crossing algorithm is used to determine ripple heights and wavelengths. Variations in bed morphology across the flume was examined through raw backscatter intensity given by the Sector Scan Sonar (SSS). Changes in bed morphology over time was inferred from the series of sequential scans within each run, taken approximately once a minute.

For the ABS records, the mean grain size and speed of sound, based on measured temperature and salinity, was used to correct backscatter for attenuation and spreading, and hence infer concentration. Thus, the one–dimensional vertical profiles of suspended sediment concentration (backscatter) and mean particle sizes could be calculated from sediment cross–section scattering of the individual sound frequencies following the methodology of (and Thorne and Hanes (2002); Thosteson and Hanes (1998)), as presented in the MATSCAT toolkit (Buscombe, 2012). The ADV records of the turbulence components are sub-sampled to match the ABS records, which, in turn, are down–sampled from 64 Hz to 25 Hz only for the cross wavelet transforms of Reynolds' stresses and synchronous suspended sediment fluxes. Given that the subsampled records displayed the same spatial and temporal properties as their original series through spectral and continuous wavelet analyses, this is believed to have no significant impact on the results.

2.3 Quadrant analysis

In a three-dimensional orthogonal system $(\mathbf{x}, \mathbf{y}, \mathbf{z})$ [where $\mathbf{x_1} = \mathbf{x_i} = \mathbf{x}$: $\mathbf{along\ flow}$; $\mathbf{x_2} = \mathbf{x_j} = \mathbf{y}$: $\mathbf{across\ flow}$; $\mathbf{x_3} = \mathbf{x_k} = \mathbf{z}$: $\mathbf{vertical}$], a Reynolds' decomposition of the instantaneous velocities ($\mathbf{U_i}$) is given by:

$$\mathbf{U_i} = \bar{\mathbf{u}}_\mathbf{i} + \mathbf{u'_i} + \mathbf{u'_{wave}} \qquad (1)$$

whereby the over-bar denotes a time-average, the prime indicates a fluctuation about the mean, and the 'wave' subscript refers to the periodic/oscillatory (wave) component. The Reynolds' stress is described by the inverse correlation between the time-average fluctuations of streamwise (u') and vertical (w') velocity components at a point:

$$\textbf{Reynolds Stress};\ \tau_{xz} = -\rho\,\overline{u'w'} \qquad (2)$$

Quadrant analysis, a technique for detecting various turbulence structures, consists of distributing streamwise and vertical velocity fluctuations into the four quadrants of the ($u'w'$) plane (Deleuze et al., 1994). Four types of structures may be distinguished: (a) an ejection/burst (E, Quadrant 2) where a low speed fluid ($u' < 0$) near the bed moves upward ($w' > 0$); (b) a sweep (S, Quadrant 4) where a high velocity fluid ($u' > 0$) moves downwards to the bed ($w' < 0$); (c) inward interactions (II, Quadrant 3) where ($u' < 0$) an ($w' < 0$); and (d) outward interactions (OI, Quadrant I) where ($u' > 0$) an ($w' > 0$). Determining the fractional contribution of each of these structural features is commonly restricted to values that lie above a critical threshold, H, whereby:

$$|u'w'| > H.\,u'_{rms}.\,w'_{rms} \qquad (3)$$

Hence, the contributions of individual events in the ($u'w'$) plane are the ones which occur in each quadrant outside the central "hole" region bounded by the four hyperbolae defined by the above inequality. However, there is no agreed definition for the threshold criterion (Blackwelder and Kaplan, 1976; Bogard and Tiederman, 1986; Keylock, 2007; Wu and Yang, 2004), and its value is chosen arbitrarily (Keylock, 2008) or ignored altogether (Keylock et al., 2014). As the threshold increases, the number of exceedances decreases, biasing the stress magnitude to be mostly contributed by ejections within the second quadrant (Keylock, 2007; Willmarth and Lu, 1972). The process outlined in (Cellino and Lemmin (2004); Longo et al. (2012); Lu and Willmarth (1973)) is used to calculate the concentrations within each quadrant. Extending quadrant analysis into three dimensions, known as Octant analysis, is less common, given that the cross–wise flow component is often assumed less important in classical flows (Gheisi et al., 2006; Keylock et al., 2014; Ölçmen et al., 2006). Quadrant/octant analysis provide a relatively simple means of characterising dominant flow structures, which can be linked to the entrainment of sediment from the bed and into suspension, and whose frequencies would dominate the velocity spectra and contribute the majority of the total shear stress (Keylock et al., 2014).

2.4 Spectral properties: Fourier and Wavelet transforms

Fourier analysis is used to study turbulent flows and identify integral scales of motion, stemming from a classical understanding of the turbulent energy cascade. This statistical view was quantified by Kolmogorov-Obukhov into the well–known $\mathbf{k^{-5/3}}$ law in the inertial subrange, with $\mathbf{k}$ denoting the wave–number for the energy spectrum in Fourier Space (Frisch, 1995; Monin and Yaglom, 1971; Tennekes and Lumley, 1972). However, the existence of organised yet stochastically intermittent eddy structures of multiple scales, varying in space and time, cannot be resolved by Fourier transforms as these transforms are inherently space-filling (Berry and Greenwood, 1975). Wavelets, on the other hand, are able to expand a time series into time-frequency space and thus determine localised intermittent periodicities (Farge, 1992; Grinsted et al., 2004), and are capable of performing efficient multi–scale decomposition (De Stefano and Vasilyev, 2012; Kumar and Foufoula-Georgiou, 1997), identifying and isolating localised structures such as vortices in physical and wave–number spaces (Farge et al., 2001; Farge et al., 2003; Khujadze et al., 2011), as well as analysing localised variations of power within a time series (Daubechies, 1990; Grinsted et al., 2004; Torrence and Compo, 1998).

A wavelet transform is in essence a linear operation which decomposes a given signal into components that appear at different scales, based on convolution of the signal with a dilated filter (Mallat, 1991). A continuous wavelet transform (CWT) decomposes a signal, $\mathbf{f(t)}$, in terms of the 'daughter' wavelets, $\boldsymbol{\psi}_{\mathbf{b,a}}\mathbf{(t)}$, derived by stretching or compressing and shifting (translating) the 'mother' wavelet, $\boldsymbol{\psi}\mathbf{(t)}$ function (Lau and Weng, 1995; Torrence and Compo, 1998). The most common mother function is the Morlet wavelet (Morlet, 1983; Morlet et al., 1982a, b), of wave vector, $\mathbf{k_\psi = 6}$, used in this work, and defined by:

$$\boldsymbol{\psi}(\mathbf{t}) = \mathbf{e}^{\mathbf{ik_\psi . t}} . \mathbf{e}^{-\frac{|\mathbf{t}|^2}{2}} \qquad (\mathbf{4})$$

The continuous and complex nature of this wavelet gives it the advantage of being able to detect both the time–dependent amplitude and phase for different frequencies in the time series (Lau and Weng, 1995). The transform maps a one dimensional time series into a two–dimensional image portraying the evolution of scales and frequencies in time (linear scale on time b–axis, and logarithmic scale on the a–axis). To speed up the transform and limit edge effects, we pad the time series with zeros, then remove these afterwards, and represent the region of spectrum where the effects may be important (near large scales) by a 'cone of influence' following (Torrence and Compo, 1998). Wavelet transforms are carried out to investigate the variability of high frequency turbulence structures and the ensuing suspension events, as well as their clustering (sequential occurrence) in time. These structures are hereby defined in terms of the Reynolds stresses as the second moment

velocity covariance (product of the turbulent components in each of the three planes). The contours of power spectra are constructed from a continuous wavelet transform of the time series of Reynolds stresses, and of the concentration time series, following the methodology of Torrence and Compo (1998) and tools presented in Grinsted et al. (2004). Finally, using cross wavelet transforms, the causality between two time-series can be scrutinized by examining whether regions in the time–frequency space with large common power have consistent phase relationships. Wavelet multi–resolution analysis is capable of detecting and tracking energetic fine–scale motions (Schneider and Vasilyev, 2010). A cross–wavelet transform (XWT) is therefore used to expose regions of high common power between the two signals of Reynolds' stresses and suspended sediment flux, looking into the phase relationships between the two (Grinsted et al., 2004).

3.0 Results and Discussions

3.1 Wave hydrodynamics and bed morphology

Eight records of erosive and accretive wave conditions (from the barrier's perspective) are analysed and presented here (four erosive sub–records taken from BARDEX II test series A3, and four accretive records from series A7 and A8). The design wave conditions, as well as calculated and measured hydrodynamic flow properties are given in Table 1. The design wave forcing in each sub-run is reproduced systematically by the paddle, with measured significant wave heights (Hs ~ 0.75 ±0.03 m in erosive, and ~0.61 ±0.07 m in accretive runs) and peak periods (Tp ~8.12 ± 0.5 s in erosive; and 12 s in accretive runs) satisfying the erosion/accretion criteria (shoreward/seaward migration of nearshore bed material) of Sunamura and Takeda (1993) for the given beach slope and mean grain size. The wave Reynolds numbers indicate turbulent rough flows (Soulsby and Clarke, 2005b), with estimated near-bed orbital velocities of $\mathbf{0.68 \pm 0.03\ m/s}$ for the erosive runs (spilling and plunging breakers with surf-similarity parameter, $\boldsymbol{\xi = 0.5 \pm, 0.012}$), and $\mathbf{0.67 \pm 0.07\ m/s}$ for the accretive runs (plunging breakers with $\boldsymbol{\xi} \cong 0.62$ (Massel, 2013)). Turbulence measurements by the two ADV's were confirmed to be taken within and outside the wave benthic boundary layer.

Within the erosive and accretive runs presented, wave-induced suborbital vortex-type ripples were observed in a bifurcating, two-dimensional configuration across and along the flume (figure 2), following the classification of (Clifton and Dingler, 1984). These were characterised by ripple height: $\mathbf{H_r}$ = 0.098 ± 0.008 m; and wavelength, $\boldsymbol{\lambda_r}$= 0.45 ± 0.09m in the erosive runs; and $\mathbf{H_r}$ = 0.10 ± 0.02 m; and $\boldsymbol{\lambda_r}$= 0.57 ± 0.06 m in the accretive runs. While certain trends in bedform growth and relaxation were observed during entire experimental

runs, only millimetric scale variations in geometry were evident within the 8-minutes long sub-records chosen for analysis of stress-suspension co-variation.

3.2 Turbulence intermittency and higher order statistics

Figure 3 shows the time series of the three instantaneous, zero-meaned velocity (U, V, and W) and inherent turbulent ($\boldsymbol{u}'$, $\boldsymbol{v}'$, and $\boldsymbol{w}'$) fluctuations, measured within and outside of the wave boundary layer (by ADV1 and ADV2 respectively) for almost the entire length of the erosive wave run A301; together with their corresponding probability distributions. The four erosive sub-records carried forward in the analysis are delimited by the vertical blue lines. Table 2 summarises the corresponding averaged statistical properties for the turbulent component of the 8-minute subsampled records from both erosive and accretive wave runs. The streamwise velocity component, $\boldsymbol{U}$, both within and outside the boundary layer, exhibits a quasi-Gaussian distribution (skewness ~ 0, kurtosis ~ 3) hinting at a stochastic process of independent probabilistic events; while the crosswise and vertical components are markedly non–Gaussian. The turbulence components are anisotropic in all three dimensions both within and outside the bottom boundary layer.

The crosswise component, commonly overlooked when analysing shear stresses in relation to sediment suspension, shows remarkably high amplitude spikes, comparable in magnitude to the streamwise flow and for a considerable amount of time, particularly near the bed. This, in turn, is reflected in a pronounced leptokurtic distribution for the transverse velocity fluctuation, which also appears to be asymmetric. The vertical velocity fluctuations are characterised by relatively high kurtosis for the erosive wave runs, and even more pronounced in the accretive runs. The is generally suggestive of a high degree of intermittency in momentum exchange. Similar results have been reported (as unexpected findings) in experimental and numerical simulations of strong boundary layers and turbulent channels, particularly in wall (bed) proximity (Choi and Guezennec, 1990; Kim et al., 1987) and at high Reynolds numbers (Kuo and Corrsin, 1971); in obstructed flow (El Khoury et al., 2010), and in viscoelastic flows (Samanta et al., 2009).

The peaked and asymmetric crosswise velocity distribution particularly near the bed has been attributed to the nearly self–similar growth and self–sustaining mechanisms of spanwise structures in close proximity to low speed regions of flow. These are often speculated to be generated by induction of the asymmetric legs of an inclined, streamwise-aligned, wall-attached horseshoe vortex structures (Adrian, 2007; Christensen and Adrian, 2001; Lozano-Duran et al., 2012; Panton, 2001; Tomkins and Adrian, 2003; Zhou et al., 1997). It has also been attributed to the more frequent occurrence, and merging, of one-

legged 'cane-like' elliptical vortices, at high Reynolds numbers (Tomkins and Adrian, 2003). The highly three–dimensional fluid entrainment process cannot be studied in the streamwise-vertical plane only, where entrainment with vortex structures is not evident (Robinson, 1991). Large streamwise vortices in wall bounded channels with moveable beds appear as secondary flows in the crosswise plane perpendicular to the streamwise flow, and affect the distribution of mean velocity, turbulence intensities, and Reynolds and bed shear stresses through the channel (Adrian and Marusic, 2012). Such eddies have been observed with a spanwise width up to 1.5 times the water depth, which oscillate slowly at the centre while forming stationary flows near the wall (Tamburrino and Gulliver, 2007). In the absence of practical means of visualising these structures in the field, we undertake quadrant analysis of the tangential stresses to assess the frequency of occurrence of sweep (Q4)–ejection (Q2) pairs as it may shed additional light on the three dimensional structure of momentum transfer near the bed (Alfredsson and Johansson, 1984; Kim et al., 1987; Lozano-Duran et al., 2012). Notably, there is no consensus as to whether the succession of ejections and sweeps creates vortices, or conversely, rolling vortices give rise to the bursting sequence, and it is plausible that both mechanisms operate cooperatively (Adrian and Marusic, 2012).

The above results emphasise the three–dimensionality of the momentum and subsequent mass exchange problem, and as such, the contributions of the three components of turbulence to momentum flux need to be considered. Subsequently, octant analyses of the three dimensional Reynolds stresses ($\boldsymbol{u'w'}, \boldsymbol{u'v'}, \boldsymbol{v'w'}$) is carried out to identify the 'active' times where momentum exchanges occur, and their fractional contributions to the overall stress. However, to remain true to the original formulation, we have opted to perform this in three distinct orthogonal planes.

3.3 Quadrant/Octant analysis and dominant structural features of flow

Quadrant analysis is used to quantify the intermittency of the instantaneous Reynolds stress signals and identify turbulence structures within a turbulent bursting sequence. Figure 4 summarises the averaged results of the quadrant analysis, performed in three planes of motion (streamwise–vertical plane ($\boldsymbol{uw}$), crosswise–vertical ($\boldsymbol{vw}$), horizontal ($\boldsymbol{uv}$)) for the erosive and accretive runs analysed. These are obtained from the four 8 minute ADV1 sub-records measured near the bed, corresponding to the ABS sampling periods in each case, without applying a threshold (Hole size, H=0). The top panel (Figure 4.a); highlights the influence of the hyperbolic hole size, H, applied as a delimiting threshold (green: H =2; grey: H=1). Notably, it was found that applying a threshold value has a far more pronounced impact in the erosive wave runs, reducing the fractional occurrence of all four types of structures by up to 80% for H=2 (most pronounced effect is on the outward (OI) and inward

(II) interactions), but only up to 30% for the accretive runs. The effect of a threshold value applied to the stresses of the accretive runs reduces the accounted motions in relatively equal proportions in any given plane (only marginal increase in the Q1 OI and sweep motions at the expense of the accounted ejections). The middle panel (Figure 4.b) presents the averaged results (of 4 sub-runs) for the erosive and accretive records, of the percentage of occurrence of each of the 4 types of bursting event structures, before and after filtering out the periodic component from the velocity fluctuations, in all three planes. The lower panel (Figure 4.c) shows the averaged percentage of contribution to stress by each of the bursting motion types, to the total Reynolds stress in the primary flow plane ($\boldsymbol{uw}$). Filtering out the periodic component appears to have a significant impact only on the proportion of time occupied by specific motions (particularly Q2 and Q3) in the dominant flow plane ($\boldsymbol{uw}$) of the erosive runs, and almost no effect in the accretive runs. It is also found that this has a negligible impact on the contribution to stress by each type of structure. For the erosive runs, Q2 (Ejection) and Q3- (Inward Interaction) motions dominate the vertical motion along ($\boldsymbol{u'w'}$ plane) and across ($\boldsymbol{v'w'}$ plane), respectively, with the wave signal present. These events entrain low speed fluid (and particulates) near the bed upwards into the water column, and highlight a prevalence of motions are directed offshore (negative $\boldsymbol{u'}$) contributing to the erosion of the barrier face. However, when considering only the fluctuating part, Q2- and Q4- motions become relatively more frequent. For the accretive wave runs, filtering out the wave signal appears to result in nearly equal proportions for each of the 4 types of motion in all planes. In the horizontal planes ($\boldsymbol{u'v'}$), Q1 and Q4 structures associated with shoreward–directed motions skewed to the right are marginally emphasised; with all motions of a bursting sequence represented relatively equally. Collectively, ejections and sweeps contribute slightly more to the total Reynolds stress (56% in erosive, 57% in accretive) than the Outward and Inward interactions. If a threshold were applied to the stresses in the erosive runs, the occurrence of Sweeps and Ejections outweighs that of the weaker interactions by a factor of 1.6 for H=2 due to the observed dominance of particular quadrant events of higher magnitude in the erosive runs, compared to the nearly equal distribution (balance) of the four quadrant event motion in the accretive tests. Remarkably, the fractional contribution of ejections and inward interactions, and hence reduced thresholds, is reportedly enhanced in sediment mixtures with high standard deviations in grain size distribution, like the coarsely skewed sediments present here; while that of the Q1 events becomes less significant (Wu and Jiang, 2007; Wu and Yang, 2004).

3.4 Spectral analysis of turbulence and suspension

Spectral analysis decomposes the measured turbulence data into waves of different periods (frequencies) and wavelengths, providing a suitable means of examining how these fluctuation are distributed from a statistical viewpoint (Tennekes and Lumley, 1972). The multitude of scales (both spatial and temporal) of turbulent eddies comprise a spectrum ranging from the macroscale (long period and spatially limited only by the dimensions of the flume/flow) to the high frequency microscale limited by viscosity, with the energy transfer being driven by vortex stretching (ibid.). The value of a spectrum at a certain frequency or wavelength equates to the mean energy of that wave, and as a result, it provides a means of assessing how eddies of different sizes exchange energy and how turbulence evolves with time. With turbulence being a largely three-dimensional problem, this necessitates construction of energy spectra in three dimensions (Cebeci and Smith, 1974) . Figure 5 shows the power spectral densities (PSD) of the three fluctuating velocity components (u'_{wave}) within and outside the boundary layer for the entire length of the erosive wave test (~ 180 minutes). These have been calculated using Welch's method with a Hann window with 50% overlap. The velocity spectra display a peak corresponding to a period of 8.19 seconds in all three components, as expected (design peak period being Tp = 8 sec). Nonetheless, a striking feature is a significant peak in the crosswise turbulence spectrum at both elevations, with a corresponding period of 2.64 seconds. This is also apparent in the accretive runs, as well as what seems to be higher order harmonics. Chu et al. (1991) have reported on unstable transverse shear flows leading to large scale turbulent motions across wide and shallow open channels (horizontal length scales significantly larger than water depth), induced by the growth of small scale disturbances induced by bed friction (critical value of 0.12–0.145) or depth variation. However, neither of these appear to be applicable in this case, given the relatively uniform cross section of the flume, and the lower wave–induced bed friction factors reported in Table 1, and some alternative mechanism must be at work.

Standing cross-waves (transverse waves) induced by symmetric wave makers in rectangular channels have been reported to occur with excitations at nearly twice one of the natural frequencies of the paddle due to nonlinear parametric resonance (Garrett, 1970; Miles, 1988). The first mode of oscillation for a rectangular channel of width, B = 5m, and water depth hs = 2.5m, occurs as half a wave with a node point at the centre of the flume, and two maxima(crests)/ minima(troughs) on either end (the rigid walls). Paterson (1983) presented the equations needed to calculate the associated wave number ($\boldsymbol{k = \pi/l}$), and angular frequency $\left(\boldsymbol{\omega = \left((\pi g/B).tanh(\pi h_s/B)\right)^{0.5}}\right)$, in which case the corresponding period in our case comes to exactly 2.64 seconds, matching perfectly the peak in the spectrum, with

higher order oscillations also observed in the spectra. The existence of a stable transverse standing wave may also be a contributor to the observed asymmetry and high kurtosis of the crosswise velocity fluctuation. Similar cross waves have been generated in much larger wave basins, such as the recent edge wave experiments at IH Cantabria (Coco, per comm.), but the existence of such waves on unconfined lengths of coast remains an open research question.

The spectra of turbulence components both within and outside the boundary layer were also constructed for each of the erosive and accretive sub-runs, following the same methodology. No significant peaks were apparent in the lower frequency range (periods longer than the peak wave period); suggesting limited effect of wave groups in the turbulence signal. When the wave signal is filtered out, no sharply-defined peaks could be attributed to the harmonics of the applied wave forcing (progressive waves along the channel); but the highest variances lie between the first harmonics of the progressive wave and the second harmonics of the transverse standing wave. This shows that the turbulent energy lies within the wave frequency range, as has been seen in studies of the inner surf zone (Ting and Kirby, 1996). Local peaks corresponding to the second harmonics of both could be discerned, indicating induced turbulence at flow reversal, often associated with the vortex shedding process. When shown in wave number space, these fluctuations approach the Kolmogorov–Obukhov $-\mathbf{5/3}$ relation within the inertial dissipation sub-range (Frisch, 1995; Stapleton and Huntley, 1995). Note, however, that spectral analysis with Fourier transforms are limited by the Nyquist frequency, limiting detected frequencies to those higher than half the sampling frequency of the instruments (Glover et al., 2011), in this case, 12.5 Hz.

Taylor's theory of "frozen turbulence" suggests that turbulence is advected by the mean current more rapidly than it is developing temporally, and as a result, the measured turbulence fluctuations at a fixed point would correspond better to the spatial rather than temporal changes in velocity (Taylor, 1938; Wyngaard and Clifford, 1977). In wavenumber ($\boldsymbol{k}$) space, where $\boldsymbol{k} = \mathbf{2}\,\boldsymbol{\pi f}/\overline{\boldsymbol{U}}$, the spectral energy for all eddies of size $\boldsymbol{2\pi/k}$ is roughly proportional to $\boldsymbol{E(k)}$ times the width of the spectrum (Tennekes and Lumley, 1972). The strain rate of an eddy is thus a function of its wavenumber, which is often scaled by the measuring height, z, into a non-dimensional form, $\boldsymbol{k}^*$. Hence, by normalising the k*-weighted spectra into an energy/variance preserving form, whereby an equal area under the curve = equal energy, it is possible to calculate the dominant eddy sizes, following (Soulsby, 1977, 1983; Soulsby et al., 1984).This was applied to the turbulence spectra, before smoothing with a moving-average algorithm, as shown in figure 6, where error bars represent standard deviation for the averaged sub-runs. The peaks indicate similar scaling in the crosswise and

vertical components near the bed for both erosive and accretive runs (~ 0.05 m), and slightly larger scales along the flow in the accretive runs (~0.18 m) as opposed to the erosive ones (~0.12 m). Along the direction of wave propagation, these vary over a range of scales higher in the water column (at ADV2) for the erosive runs (between 0.1 – 0.3 m), and increase substantially in the accretive ones (~1 m streamwise, 0.2 m in the crosswise and vertical). The vertical excursions scale well with the wave boundary layer thickness in both erosive and accretive runs. Overall, the wavenumbers contributing to horizontal motions are smaller than those contributing the vertical motions.

The power spectral densities of sediment backscatter at 5 elevations above the bed are presented in figure 7, for all of the analysed sub-runs. The suspension spectra in both erosive and accretive runs exhibit multiple or broad peaks near the bed and higher in the water column, with frequencies corresponding to the second harmonics of the progressive waves, as well those of the transverse waves. This implies suspension of sediment is associated with the shedding of vortices from bedforms within the boundary layer (O'hara Murray et al., 2011), and extending much higher in the water column, potentially due to pairing of vortices (Williams et al., 2007). This claim is supported by the bed morphology, stable, 2D vortex ripples with no considerable migration over the duration of each 8 minute sub-run. It does not appear, however, that wave groups play a role in this case, as has been reported in irregular waves over evolving bedforms (O'hara Murray et al., 2012). The peaks corresponding to the transverse wave properties highlight the nonlinearity and three dimensionality of the sediment suspension process, both in terms of sediment pick up and maintenance of suspension higher in the water column. While the spectra in the lower frequency range are steeper near the bed, and relatively flatter higher up, these trends reverse at the higher frequency scales. This may suggest that the stirring of sediment near the bed is driven by the mean flow properties, but the waves do not play a significant role in retaining sediment in suspension. Steeper slopes of energy spectra at higher frequencies are often associated with coherent structures (Maltrud and Vallis, 1991), and as such, higher frequency turbulence may be the dominant mechanism at work at higher elevations above the bed, and hence key to modelling suspension of sediment outside the boundary layer.

The time dependency between the horizontal shear stress and sediment concentration also varies with elevation (Venditti and Bennett, 2000). Given the existence of an undertow in this case (~ 0.2 m/s offshore), vertical variations are expected in spilling breakers (erosive runs) as turbulence gradually spread downwards by moderate scale eddies from the surface roller, but not in plunging breakers where downward generated large scale vortices create strong vertical mixing (Ting and Kirby, 1994, 1996). Plunging breakers are dominated by orbital

wave motion and turbulence is thus convected landwards, favouring accretion and indicating strong dependence on history downstream, while spilling breakers are dominated by the undertow moving sediments seaward (ibid.).

The erosion process, locally, is likely to be affected by the passage of large scale coherent structures with low occurrence probability (Adrian and Marusic, 2012), and there is growing evidence that the concept of bursting as a violent ejection is replaced by the concept of "slowly evolving" fast packets of vortices creating sequences of ejecting/sweeping events each associated with one of the vortices (Christensen and Adrian, 2001; Jimenez, 2012; Jiménez, 2013). We conjecture that the succession of convected or locally generated intermittent bursting or sweeping motions would dictate whether the entrained sediment has enough time to settle, is amplified by added suspensions, or swept back to the bed. This governs the frequency response of suspension events and how they interfere with turbulent fluctuations. Wavelet analysis may offer some clues as it provides information not only on frequency scales, but their spatial (occurrence in time) variability too. Whether erosion or accretion is observed at the barrier is then governed by the mean currents which could transport the agitated sediments above the bed. This is typical of a stochastic process where particle concentration is closely related to that of the turbulence fluctuation arising from large eddies as shown in the work of (Liu et al., 2012). Such episodic events could occur at any location of the bed, with short periods of considerable sediment movement intermingled with long periods of negligible transport (Dey et al., 2012).

3.5 Wavelet analysis of Reynolds' stresses and sediment resuspension

Figure 8 shows the power spectra highlighting time-frequency characteristics of the three Reynolds' stresses and sediment suspension obtained through continuous wavelet transforms for an example sub-run from the erosive series. Matching results are evident in the other runs (not shown for brevity), and the behaviour reported hereafter is true for both erosive and accretive runs. In this figure, the left panels pertain to measurements at the level of ADV1 (within the wave boundary layer), while results from measurements corresponding to ADV2 (outside the boundary layer) are displayed on the right panels. The figure shows the time series of the three Reynolds' stresses in 3 orthogonal planes of motion: ($\boldsymbol{u'w'}$) in the streamwise-vertical plane (bed normal along the direction of wave propagation), ($\boldsymbol{u'v'}$) in the horizontal plane, and ($\boldsymbol{v'w'}$) in the crosswise-vertical plane, having filtered out the wave-signal from the fluctuating turbulence components, as well as their energy spectra (obtained by Fourier transforms, as discussed in section §2.4. The time-series of continuous wavelet transforms (CWT) for each of the stresses in the time-frequency domain, are presented subsequently in the same order, together with their global spectral power (integrated

variance). We opted to present the inverse frequencies (i.e. periods) on the vertical axes, to facilitate the discussion when related to wave properties. The global power pertains to time averages, if we were to take a vertical slice through the wavelet plot, and average all the local wavelet spectra (Torrence and Compo, 1998).

Finally, the lower two panels show the time series of vertical suspension (logarithmic backscatter, higher values in warmer colours) profiles below the ABS sensor head, the power spectral densities of suspended sediment concentration at the level of the corresponding ADV (ADV1 on the left, ADV2 on the right), and the related continuous wavelet transform of the suspension time series at that elevation, together with its global spectral power. In these plots, warmer colours indicate higher power (variance), the white-shaded region represents the cone of influence where edge effects may distort the image, and the thick contours represent the 95% confidence limit (5% significance against red noise). Note that at higher periods (low frequency events), the power falls within the cone of influence, limiting our ability to investigate the temporal evolution of the particular peak frequencies reported in section §2.4. Therefore, we are restricted to investigating very high frequency events occurring at time scales up to 2 seconds. This limitation arises from Heisenberg's uncertainty principle, which dictates that one cannot obtain arbitrary good localisation in both time and frequency, and a trade–off must exist whereby spatial resolution is bad at large scales while scale (frequency) resolution is bad in the small scales (Farge et al., 1996; Foufoula-Georgiou and Kumar, 1994; Grinsted et al., 2004; Lau and Weng, 1995). Having said that, it is clear that most of the power (variance) in concentration lies within the lower frequency range (high period) associated with the mean flow properties for both stresses and suspensions near the bed.

The Fourier-transform-derived spectra of Reynolds stresses show that they approach the universal Kolmogorov–Obukhov -5/3 relation corresponding to the inertial dissipation sub-range (Frisch, 1995, Stapleton and Huntley, 1995). While this is still true for stresses measured outside the boundary layer (by ADV2), it is interesting that a secondary peak appears within the higher frequency range, suggesting enhanced turbulence with smaller scales of motion. The CWT results show that 'powerful' (i.e. high variance) turbulent events occur intermittently throughout the records, in slowly evolving clusters that persist over short times in the dominant flow direction (streamwise-vertical) near the bed, and for longer times (significant from a turbulence perspective, up to several minutes), higher up in the water column, and at lower frequencies. The larger clusters fall over short bands of frequency scales (specific periods, predominantly 0.5 and 2 seconds); while the fast-evolving clusters extend over a bigger range of frequency scales (primarily between ½ and 1/64 seconds)

before diminishing. This may indicate breakup of the larger eddies into smaller and smaller ones within the inertial dissipation range, before the energy is consumed by viscosity, as described by the classical turbulence cascade which suggests that inertia results in stretching and rapid breakup of vortices into many smaller, excited degrees of freedom, until energy is dissipated through viscosity (Frisch, 1995; Kolmogorov, 1991; Sreenivasan and Antonia, 1997; Tennekes and Lumley, 1972). The turbulent clusters within the streamwise-vertical plane (hereafter referred to as the dominant plane of motion) have the highest power, which appears to be uniformly distributed across the aforementioned frequency range. In the horizontal plane, such events are also considerably powerful, but tend to spike closer to the lower end of the range, at periods comparable to the harmonics of the transverse standing wave. In the crosswise-vertical plane, significant clusters of turbulent stresses occur for longer times, but their power is negligible compared to those of the other two planes of motion.

Periods associated with a succession of powerful turbulent events are very closely followed by periods of powerful, high frequency suspensions, extending from the larger scales observed in the low frequency range (periods up to 4 seconds/outside the cone of influence), and exponentially extending over smaller and smaller scales (higher frequencies/lower periods) before decaying as turbulence clusters cease. This may be explained as cumulative, highly-varied suspensions in response to the faster turbulent perturbations, where continuing upward diffusions exceeds the settling velocity of the entrained particles. Even the more sporadic suspension events of lower significance appear to conform to the aforementioned behaviour, if the wave signal is not excluded from the turbulent fluctuation (shown in Figure 9). Comparing the two figures shows that the bulk of sediment suspension events can be attributed to wave-induced turbulent fluctuations of low frequency (only higher order harmonics of the wave period (4/Tp) are visible outside the cone), where most of the global power is retained. Yet, the short-lasting suspension clusters scale with the rapidly decaying high frequency turbulence. This perhaps highlights a hysteresis effect, where a dynamic lag occurs between the driving mechanism in terms of the formation, and evolution of a vortex structure and ensuing bursting sequence, and the response in terms of sediment resuspension. These periods of high power and long suspension events often appear directly following significantly large amplitude variations in water surface elevation of up to 1.4 m, inferred from the pressure gauge (not shown here). This suggests that the initiation of a large suspension event beyond the mean flow frequency range is instigated by the passage of the more energetic waves within the JONSWAP spectrum, or with early wave breaking events. Its persistence in the higher frequency range is then dictated by the supply of fluid momentum; either generated through bed friction, or injected downwards by the

spilling breakers of these erosive wave runs. Higher in the water column, few suspension events are observed at the high frequencies, and where they do occur, these are characterised by a rapid expanse of the scales followed by rapid decay (dissipation of energy). In the accretionary runs, the turbulence events span even wider scales and occur over longer times, corresponding to significant fluctuations in the time series of the turbulence components (and water elevation). These clusters can be interpreted as large scale, uniform momentum regions convected or formed near the bed in the low frequency range. As they evolve, they cause small scales vortices that experience sudden and short lived changes in velocity, manifest by short duration events of high variance, that appear to be 'shooting out' of the larger clusters and spanning a significant extent in the high frequency range in these plots. This change can cause higher shear stresses compared with the mean flow, as reported by (Hutchins et al., 2011; Mathis et al., 2011), and as such, are often followed by significant suspension clusters.

To examine the hypothesis thus posited, cross-wavelet transforms (XWT) of the Reynolds stresses in three planes, and the recorded suspended sediment concentrations are presented in Figures 10, both within and outside the wave boundary layer. Note that this can only be done after down-sampling the 64 Hz suspension record to match the sampling frequency (25 Hz) of the ADVs. The significance levels are tested against red noise generated by a first order autoregressive model following Grinsted et al. (2004), and denoted by the thick contours. The lightly shaded area represents the cone of influence. The XWT has been applied to the turbulent fluctuations before (denoted by the "wave" subscript); and after filtering out the wave signal for each of the Reynolds' stresses in every plane. The phase relationship between the two signals (stress and concentration) is shown by the arrows, whereby right arrows indicate signals are in-phase, left-pointing arrows indicate anti-phase, and vertical arrows suggest that the Reynolds stresses lead concentration by 90 degrees phase shift, testing the coherence of the transform (Grinsted et al., 2004). Here we notice common features as observed in Figures 8 and 9, where suspension events and turbulent stresses share high common power at a range of scales. At the smaller frequency scales, these regions of significant common power occur for most of the time near the bed and in all three planes, particularly when the wave signal is present, albeit falling within the cone of influence. The powerful events at lower periods of 2 – 4 seconds are phase locked, implying causality between the wave-induced turbulence and the ensuing suspension, but with no notion of time lag. However, no robust measure of whether this may be an artefact of the dominance of one of the signals, or not, is carried out (e.g. combining clustered wavelet spectra with maximum covariance analysis presented by Rouyer et al. (2008)). The higher-frequency 'wave-contaminated' scales appear to be less coherent in all planes both near the

bed and outside the boundary layer. However, once the wave signal is filtered out, the turbulent fluctuations outside the boundary layer appear to be predominant in driving the suspensions at this level, with the highest power, although being phase-locked in the opposite direction.

Nonetheless, the wavelet analyses presented collectively support the conjecture proposed, postulating a mechanism in which successive intermittent bursting motions play a significant role in moving and maintaining sediments in suspension. In time-frequency space, it is shown how most of the momentum exchange, and ensuing suspension, lies within the low frequency range (high periods) dictated by the mean flow properties. The passage of intermittent and relatively large momentum regions of uniform spectral properties at higher frequencies, plays a direct role in sediments suspensions which exhibit significant variability within the higher frequency range. As these regions, which signify the passage of a coherent structures, persist for a considerable amount of time, suspensions near the bed are amplified before decaying as the supply of momentum by these turbulent structures ceases. Within a given cluster of turbulence, both stresses and suspensions span a certain range of frequencies, which may hint at a nonlinear modulation of both the amplitude and frequency of such small structures with the larger flow structures near the bed. Such behaviour in wall turbulence has been attributed to local changes in shear but not necessarily the spatial and temporal structure of large flow events (Ganapathisubramani et al., 2012).

4.0 Conclusions

The aim of this study was to provide insight into the temporal and scale relationships between wave–generated boundary layer turbulence and event–driven sediment transport in oscillatory flow. The work was carried out in the nearshore of a prototype sandy barrier beach using data collected though the BARDEX II experiments for irregular erosive and accretive wave conditions. Statistical analysis of the time series of velocity fluctuations show high anisotropy in the turbulence records, with strikingly peaky crosswise distributions and an intermittent nature of the momentum exchange. Quadrant analysis quantified the intermittency of Reynolds stresses in three planes. The fractional contribution to stress in terms of occurrence times reveal the dominance of shoreward directed motions in accretionary waves, and sweeping motion seawards under erosive conditions; as well as a tendency to move sediments to one side of the channel, as observed in the skewness in the turbulence records. Spectral analysis further reveal a contribution to the crosswise velocity fluctuations from a standing transverse waves across the flume, resulting from the unique flume geometry, whose signal was reflected in the suspension records. The entrainment and maintenance of sediments in suspension through the bursting sequence is conjectured to be

associated with the passage of convected or locally formed packets of eddies which describe intermittent large coherent structures within the flow. Wavelet analysis further confirmed that powerful (high variance) turbulence occurred in slowly evolving clusters over time, which were closely followed by periods of powerful suspensions near the bed, emerging from the integral (dominant) scales at low frequencies, and decaying with memory in time, after the cessation of the turbulent perturbation. The larger wave-induced motions and nearbed suspension are phase-locked in the lower frequency range, suggesting that waves acts to stir up and initiate entrainment of sediment in the boundary layer. Outside the boundary layer, turbulent fluctuations are dominant in driving and maintaining high frequency suspensions as long as momentum is supplied. In summary:

a- Turbulence in irregular oscillatory flow is highly anisotropic, and characterised by intermittent momentum exchanges, describing a spatially varied bursting sequence which may be traced in three dimensions, and the temporal variability of which dictates the net direction of sediment transport in erosive and accretive runs.

b- The bursting sequence is associated with the passage of large scale slowly evolving structures, which can modulate the frequency of small scale (higher frequency) events. The persistence of such perturbations is associated with a cumulative suspension events spanning the frequency scales, which observe a hysteresis effect decaying as the motion cease. Wave motion plays a dominant role in entrainment of sediment within the boundary layer, and high frequency turbulence resulting from momentum transfer into smaller scales helps maintain particles in suspension.

c- Flume studies of turbulence and sediment transport must consider the effect of flow geometry which may induce artefact hydrodynamics that can significantly have an influence on the processes being investigated. The transverse standing wave reported in this study is a case in point, whereby a secondary process at work was evident in the statistical and spectral properties of turbulence and suspension events observed.

Artwork and Tables

Attached at the end, and separately.

Acknowledgements

The data reported here were collected in the Delta Flume, Deltares (The Netherlands) as part of the EU-funded Barrier Dynamics Experiments II – BARDEX II project (HYDRALAB IV Contract no. 261520 by the European Community's Seventh Framework Programme). Special thanks are due to Dr Gerald Muller for information on transverse standing waves. The work reported here forms part of the first author's PhD research, jointly funded by the Graduate School at National Oceanography Centre, Southampton; Faculty of Engineering and the Environment; University of Southampton; Southampton Marine and Maritime Institute; and HR Wallingford ltd.

List of References

Aagaard, T., Hughes, M.G., 2010. Breaker turbulence and sediment suspension in the surf zone. Marine Geology 271, 250-259.
Aagaard, T., Jensen, S.G., 2013. Sediment concentration and vertical mixing under breaking waves. Marine Geology 336, 146-159.
Adrian, R.J., 2007. Hairpin vortex organization in wall turbulence. Phys Fluids 19, 41301-41301- 41301-41316.
Adrian, R.J., Marusic, I., 2012. Coherent structures in flow over hydraulic engineering surfaces. Journal of Hydraulic Research 50, 451-464.
Alfredsson, P.H., Johansson, A.V., 1984. On the detection of turbulence-generating events. J Fluid Mech 139, 325-345.
Amoudry, L.O., Bell, P.S., Thorne, P.D., Souza, A.J., 2013. Toward representing wave-induced sediment suspension over sand ripples in RANS models. Journal of Geophysical Research: Oceans, n/a-n/a.
Bagnold, R.A., Taylor, G., 1946. Motion of Waves in Shallow Water. Interaction between Waves and Sand Bottoms. Proceedings of the Royal Society of London. Series A. Mathematical and Physical Sciences 187, 1-18.

Bennett, S.J., Bridge, J.S., Best, J.L., 1998. Fluid and sediment dynamics of upper stage plane beds. Journal of Geophysical Research: Oceans 103, 1239-1274.
Berry, M.V., Greenwood, D.A., 1975. On the ubiquity of the sine wave. American Journal of Physics 43, 91-91.
Blackwelder, R.F., Kaplan, R.E., 1976. On the wall structure of the turbulent boundary layer. J Fluid Mech 76, 89-112.
Bogard, D.G., Tiederman, W.G., 1986. Burst detection with single-point velocity measurements. J Fluid Mech 162, 389-413.
Buscombe, D., 2012. MATSCAT version 1: MATLAB Toolbox for the Aquascat 1000 Acoustic Backscatter Sensor., Technical report for the School of Marine Scienceand Engineering. Plymouth University., p. 6.
Cao, Z., 1997. Turbulent Bursting-Based Sediment Entrainment Function. Journal of Hydraulic Engineering 123, 233-236.
Carstensen, S., Sumer, B.M., Fredsoe, J., 2010. Coherent structures in wave boundary layers. Part 1. Oscillatory motion. J Fluid Mech 646, 169-206.
Carstensen, S., Sumer, B.M., Fredsøe, J., 2012. A note on turbulent spots over a rough bed in wave boundary layers. Physics of Fluids (1994-present) 24, -.
Cebeci, T., Smith, A.M.O., 1974. Analysis of turbulent boundary layers. Academic Press, New York ; London.
Cellino, M., Lemmin, U., 2004. Influence of Coherent Flow Structures on the Dynamics of Suspended Sediment Transport in Open-Channel Flow. Journal of Hydraulic Engineering 130, 1077-1088.
Choi, W.C., Guezennec, Y.G., 1990. On the asymmetry of structures in turbulent boundary layers. Physics of Fluids A: Fluid Dynamics (1989-1993) 2, 628-630.
Christensen, K.T., Adrian, R.J., 2001. Statistical evidence of hairpin vortex packets in wall turbulence. J Fluid Mech 431, 433-443.
Chu, V., Wu, J., Khayat, R., 1991. Stability of Transverse Shear Flows in Shallow Open Channels. Journal of Hydraulic Engineering 117, 1370-1388.
Clifton, H.E., Dingler, J.R., 1984. Wave-Formed Structures and Paleoenvironmental Reconstruction, in: Greenwood, B., Davis, R.A. (Eds.), Developments in Sedimentology. Elsevier, pp. 165-198.
Daubechies, I., 1990. The wavelet transform, time-frequency localization and signal analysis. Information Theory, IEEE Transactions on 36, 961-1005.
De Stefano, G., Vasilyev, O.V., 2012. A fully adaptive wavelet-based approach to homogeneous turbulence simulation. J Fluid Mech 695, 149-172.
Deleuze, J., Audiffren, N., Elena, M., 1994. Quadrant analysis in a heated-wall supersonic boundary layer. Physics of Fluids (1994-present) 6, 4031-4041.
Dey, S., Das, R., Gaudio, R., Bose, S., 2012. Turbulence in mobile-bed streams. Acta Geophys. 60, 1547-1588.
Dyer, K.R., Soulsby, R.L., 1988. Sand Transport on the Continental Shelf. Annual Review of Fluid Mechanics 20, 295-324.
El Khoury, G.K., Pettersen, B., Andersson, H.I., Barri, M., 2010. Asymmetries in an obstructed turbulent channel flow. Physics of Fluids (1994-present) 22, -.
Elgar, S., Raubenheimer, B., Guza, R.T., 2001. Current Meter Performance in the Surf Zone*. Journal of Atmospheric and Oceanic Technology 18, 1735-1746.
Elgar, S., Raubenheimer, B., Guza, R.T., 2005. Quality control of acoustic Doppler velocimeter data in the surfzone. Measurement Science and Technology 16, 1889.
Farge, M., 1992. Wavelet Transforms and their Applications to Turbulence. Annual Review of Fluid Mechanics 24, 395-458.
Farge, M., Kevlahan, N., Perrier, V., Goirand, E., 1996. Wavelets and turbulence. Proceedings of the IEEE 84, 639-669.
Farge, M., Pellegrino, G., Schneider, K., 2001. Coherent Vortex Extraction in 3D Turbulent Flows Using Orthogonal Wavelets. Phys Rev Lett 87, 054501.

Farge, M., Schneider, K., Pellegrino, G., Wray, A.A., Rogallo, R.S., 2003. Coherent vortex extraction in three-dimensional homogeneous turbulence: Comparison between CVS-wavelet and POD-Fourier decompositions. Physics of Fluids (1994-present) 15, 2886-2896.
Feddersen, F., 2010. Quality Controlling Surf Zone Acoustic Doppler Velocimeter Observations to Estimate the Turbulent Dissipation Rate. Journal of Atmospheric and Oceanic Technology 27, 2039-2055.
Fiedler, H.E., 1988. Coherent structures in turbulent flows. Prog. Aerosp. Sci. 25, 231-269269.
Foufoula-Georgiou, E., Kumar, P., 1994. Wavelets in geophysics. Academic Press, San Diego, CA.
Frisch, U., 1995. Turbulence : the legacy of A.N. Kolmogorov. Cambridge University Press, Cambridge.
Ganapathisubramani, B., Hutchins, N., Monty, J.P., Chung, D., Marusic, I., 2012. Amplitude and frequency modulation in wall turbulence. J Fluid Mech 712, 61-91.
Garrett, C.J.R., 1970. On cross-waves. J Fluid Mech 41, 837-849.
Gheisi, A., Alavimoghaddam, M., Dadrasmoghaddam, A., 2006. Markovian–Octant analysis based stable turbulent shear stresses in near-bed bursting phenomena of vortex settling chamber. Environmental Fluid Mechanics 6, 549-572.
Glover, D.M., Jenkins, W.J., Doney, S.C., 2011. Modeling methods for marine science. Cambridge University Press ;, Cambridge.
Goring, D., Nikora, V., 2002. Despiking Acoustic Doppler Velocimeter Data. Journal of Hydraulic Engineering 128, 117-126.
Goring, D., Nikora, V., 2003. Closure to “Depiking Acoustic Doppler Velocimeter Data” by Derek G. Goring and Vladimir I. Nikora. Journal of Hydraulic Engineering 129, 487-488.
Grigoriadis, D.G.E., Balaras, E., Dimas, A.A., 2013. Coherent Structures in Oscillating Turbulent Boundary Layers Over a Fixed Rippled Bed. Flow Turbulence Combust 91, 565-585.
Grinsted, A., Moore, J.C., Jevrejeva, S., 2004. Application of the cross wavelet transform and wavelet coherence to geophysical time series. Nonlin. Processes Geophys. 11, 561-566.
Hardy, R.J., Best, J.L., Lane, S.N., Carbonneau, P.E., 2010. Coherent flow structures in a depth-limited flow over a gravel surface: The influence of surface roughness. Journal of Geophysical Research: Earth Surface 115, F03006.
Hare, J., Hay, A.E., Zedel, L., Cheel, R., 2014. Observations of the space-time structure of flow, turbulence, and stress over orbital-scale ripples. Journal of Geophysical Research: Oceans, n/a-n/a.
Heathershaw, A., 1974. “Bursting” phenomena in the sea. Nature 248, 394 - 395.
Heathershaw, A.D., 1979. The turbulent structure of the bottom boundary layer in a tidal current. Geophysical Journal of the Royal Astronomical Society 58, 395-430.
Hussain, A., 1986. Coherent Structures and Turbulence. J Fluid Mech 173, 303-356.
Hussain, A.K.M.F., 1983. Coherent structures—reality and myth. Physics of Fluids (1958-1988) 26, 2816-2850.
Hutchins, N., Monty, J.P., Ganapathisubramani, B., NG, H.C.H., Marusic, I., 2011. Three-dimensional conditional structure of a high-Reynolds-number turbulent boundary layer. J Fluid Mech 673, 255-285.
Ji, C., Munjiza, A., Avital, E., Ma, J., Williams, J.J.R., 2013. Direct numerical simulation of sediment entrainment in turbulent channel flow. Phys Fluids 25, 056601-056620.
Jimenez, J., 2012. Cascades in Wall-Bounded Turbulence, in: Davis, S.H., Moin, P. (Eds.), Annu Rev Fluid Mech. Annual Reviews, Palo Alto, pp. 27-45.
Jiménez, J., 2013. Near-wall turbulence. Physics of Fluids (1994-present) 25, -.
Kawanisi, K., Yokosi, S., 1993. Measurements of Turbulence and Suspended Sediment in Tidal River. Journal of Hydraulic Engineering 119, 704-724.
Keylock, C.J., 2007. The visualization of turbulence data using a wavelet-based method. Earth Surface Processes and Landforms 32, 637-647.

Keylock, C.J., 2008. A criterion for delimiting active periods within turbulent flows. Geophys Res Lett 35, L11804.
Keylock, C.J., Lane, S.N., Richards, K.S., 2014. Quadrant/octant sequencing and the role of coherent structures in bed load sediment entrainment. Journal of Geophysical Research: Earth Surface 119, 2012JF002698.
Khujadze, G., Nguyen van yen, R., Schneider, K., Oberlack, M., Farge, M., 2011. Coherent vorticity extraction in turbulent boundary layers using orthogonal wavelets. Journal of Physics: Conference Series 318, 022011.
Kim, J., Moin, P., Moser, R., 1987. Turbulence statistics in fully developed channel flow at low Reynolds number. J Fluid Mech 177, 133-166.
Kline, S.J., Reynolds, W.C., Schraub, F.A., Runstadler, P.W., 1967. The structure of turbulent boundary layers. J Fluid Mech 30, 741.
Kolmogorov, A.N., 1991. Dissipation of Energy in the Locally Isotropic Turbulence. Proceedings of the Royal Society A: Mathematical, Physical and Engineering Science 434, 15-17.
Kumar, P., Foufoula-Georgiou, E., 1997. Wavelet analysis for geophysical applications. Reviews of Geophysics 35, 385-412.
Kuo, A.Y.-S., Corrsin, S., 1971. Experiments on internal intermittency and fine-structure distribution functions in fully turbulent fluid. J Fluid Mech 50, 285-319.
Lau, K.M., Weng, H., 1995. Climate Signal Detection Using Wavelet Transform: How to Make a Time Series Sing. Bulletin of the American Meteorological Society 76, 2391-2402.
Laufer, J., 1975. New Trends in Experimental Turbulence Research. Annual Review of Fluid Mechanics 7, 307-326.
Liu, J., Wang, Y., Yang, B., 2012. Wavelet packet analysis of particle response to turbulent fluctuation. Advanced Powder Technology 23, 305-314.
Longo, S., Chiapponi, L., Clavero, M., Makela, T., Liang, D.F., 2012. Study of the turbulence in the air-side and water-side boundary layers in experimental laboratory wind induced surface waves. Coast Eng 69, 67-81.
Lozano-Duran, A., Flores, O., Jimenez, J., 2012. The three-dimensional structure of momentum transfer in turbulent channels. J Fluid Mech 694, 100-130.
Lu, S.S., Willmarth, W.W., 1973. Measurements of the structure of the Reynolds stress in a turbulent boundary layer. J Fluid Mech 60, 481-511.
Mallat, S., 1991. Zero-crossings of a wavelet transform. Information Theory, IEEE Transactions on 37, 1019-1033.
Maltrud, M.E., Vallis, G.K., 1991. Energy spectra and coherent structures in forced two-dimensional and beta-plane turbulence. J Fluid Mech 228, 321-342.
Massel, S.R., 2013. Ocean Surface Waves - Their Physics and Prediction Second ed. World Scientific, Singapore.
Masselink, G., Turner, I.L., Conley, D.C., Ruessink, G., Matias, A., Thompson, C., Castelle, B., Wolters, G., 2013. BARDEX II: Bringing the beach to the laboratory–again! In: Conley, D.C., Masselink, G., Russell, P.E. and O'Hare, T.J. (eds.), Proceedings 12th International Coastal Symposium,. Journal of Coastal Research, 1545 - 1550.
Mathis, R., Marusic, I., Hutchins, N., Sreenivasan, K.R., 2011. The relationship between the velocity skewness and the amplitude modulation of the small scale by the large scale in turbulent boundary layers. Physics of Fluids (1994-present) 23, -.
Miles, J., 1988. Parametrically excited, standing cross-waves. J Fluid Mech 186, 119-127.
Monin, A.S., Yaglom, A.M., 1971. Statistical fluid mechanics; mechanics of turbulence, English ed. MIT Press, Cambridge, Mass.
Mori, N., Suzuki, T., Kakuno, S., 2007. Noise of Acoustic Doppler Velocimeter Data in Bubbly Flows. Journal of Engineering Mechanics 133, 122-125.
Morlet, J., 1983. Sampling Theory and Wave Propagation, in: Chen, C.H. (Ed.), Issues in Acoustic Signal — Image Processing and Recognition. Springer Berlin Heidelberg, pp. 233-261.

Morlet, J., Arens, G., Fourgeau, E., Giard, D., 1982a. Wave propagation and sampling theory; Part I, Complex signal and scattering in multilayered media. Geophysics 47, 203-221.
Morlet, J., Arens, G., Fourgeau, E., Giard, D., 1982b. Wave propagation and sampling theory; Part II, Sampling theory and complex waves. Geophysics 47, 222-236.
Nielsen, P., 1992. Coastal bottom boundary layers and sediment transport. World Scientific, Singapore.
O'Hara Murray, R.B., Hodgson, D.M., Thorne, P.D., 2012. Wave groups and sediment resuspension processes over evolving sandy bedforms. Cont Shelf Res 46, 16-30.
O'Hara Murray, R.B., Thorne, P.D., Hodgson, D.M., 2011. Intrawave observations of sediment entrainment processes above sand ripples under irregular waves. Journal of Geophysical Research: Oceans 116, C01001.
Offen, G.R., Kline, S.J., 1974. Combined Dye-Streak and Hydrogen-Bubble Visual Observations of a Turbulent Boundary-Layer. J Fluid Mech 62, 223-&.
Offen, G.R., Kline, S.J., 1975. Proposed Model of Bursting Process in Turbulent Boundary-Layers. J Fluid Mech 70, 209-228.
Okamoto, N., Yoshimatsu, K., Schneider, K., Farge, M., Kaneda, Y., 2007. Coherent vortices in high resolution direct numerical simulation of homogeneous isotropic turbulence: A wavelet viewpoint. Physics of Fluids (1994-present) 19, -.
Ölçmen, S.M., Simpson, R.L., Newby, J.W., 2006. Octant analysis based structural relations for three-dimensional turbulent boundary layers. Physics of Fluids (1994-present) 18, -.
Panton, R.L., 2001. Overview of the self-sustaining mechanisms of wall turbulence. Prog. Aerosp. Sci. 37, 341-383.
Paterson, A.R., 1983. A first course in fluid dynamics. Cambridge University Press, Cambridge.
Robinson, S.K., 1991. Coherent Motions in the Turbulent Boundary Layer. Annual Review of Fluid Mechanics 23, 601-639.
Rouyer, T., Fromentin, J., Stenseth, N., Cazelles, B., 2008. Analysing multiple time series and extending significance testing in wavelet analysis. Marine Ecology Progress Series 359, 11-23.
Samanta, G., Housiadas, K.D., Handler, R.A., Beris, A.N., 2009. Effects of viscoelasticity on the probability density functions in turbulent channel flow. Physics of Fluids (1994-present) 21, -.
Schneider, K., Vasilyev, O.V., 2010. Wavelet Methods in Computational Fluid Dynamics. Annual Review of Fluid Mechanics 42, 473-503.
Schoppa, W., Hussain, F., 2002. Coherent structure generation in near-wall turbulence. J Fluid Mech 453, 57-108.
Soulsby, R.L., 1977. Similarity Scaling of Turbulence Spectra in Marine and Atmospheric Boundary Layers. Journal of Physical Oceanography 7, 934-937.
Soulsby, R.L., 1983. Chapter 5 The Bottom Boundary Layer of Shelf Seas, in: Johns, B. (Ed.), Elsevier Oceanography Series. Elsevier, pp. 189-266.
Soulsby, R.L., Clarke, S., 2005a. Bed Shear-Stresses Under Combined Waves and Currents on Smooth and Rough Beds. HR Wallingford, Wallingford, UK, p. 22.
Soulsby, R.L., Clarke, S., 2005b. Bed Shear stress under combined waves and currents on smooth and rough beds.
Soulsby, R.L., Humphery, J.D., 1990. Field Observations of Wave-Current Interaction at the Sea Bed, in: Tørum, A., Gudmestad, O.T. (Eds.), Water Wave Kinematics. Springer Netherlands, pp. 413-428.
Soulsby, R.L., Salkield, A.P., Le Good, G.P., 1984. Measurements of the turbulence characteristics of sand suspended by a tidal current. Cont Shelf Res 3, 439-454.
Sreenivasan, K.R., Antonia, R.A., 1997. The phenomenology of small-scale turbulence. Annual Reviews.
Stapleton, K.R., Huntley, D.A., 1995. Seabed stress determinations using the inertial dissipation method and the turbulent kinetic energy method. Earth Surface Processes and Landforms 20, 807-815.

Sunamura, T., Takeda, I., 1993. Bar movement and shoreline change: Predictive relations. Journal of Coastal Research 15, 125-140.
Tamburrino, A., Gulliver, J.S., 2007. Free-surface visualization of streamwise vortices in a channel flow. Water Resources Research 43, W11410.
Taylor, G.I., 1938. The Spectrum of Turbulence. Proceedings of the Royal Society of London. Series A - Mathematical and Physical Sciences 164, 476-490.
Tennekes, H., Lumley, J.L., 1972. A first course in turbulence. MIT Press, Cambridge, Mass.
Thompson, C.E.L., Couceiro, F., Fones, G.R., Helsby, R., Amos, C.L., Black, K., Parker, E.R., Greenwood, N., Statham, P.J., Kelly-Gerreyn, B.A., 2011. In situ flume measurements of resuspension in the North Sea. Estuar Coast Shelf S 94, 77-88.
Thompson, C.E.L., Kassem, H., Williams, J.J., 2013. BARDEX II: Nearshore sediment resuspension and bed morphology, in: Conley, D.C., Masselink, G., Russell, P.E., O'Hare, T.J. (Eds.), 12th International Coastal Symposium Journal of Coastal Research, Plymouth, England, pp. 1593 - 1598.
Thompson, C.E.L., Williams, J.J., Metje, N., Coates, L.E., Pacheco, A., 2012. Turbulence based measurements of wave friction factors under irregular waves on a gravel bed. Coast Eng 63, 39-47.
Thorne, P.D., Davies, A.G., Williams, J.J., 2003. Measurements of near-bed intra-wave sediment entrainment above vortex ripples. Geophys Res Lett 30, 2028.
Thorne, P.D., Hanes, D.M., 2002. A review of acoustic measurement of small-scale sediment processes. Cont Shelf Res 22, 603-632.
Thosteson, E.D., Hanes, D.M., 1998. A simplified method for determining sediment size and concentration from multiple frequency acoustic backscatter measurements. The Journal of the Acoustical Society of America 104, 820-830.
Ting, F.C.K., Kirby, J.T., 1994. Observation of undertow and turbulence in a laboratory surf zone. Coast Eng 24, 51-80.
Ting, F.C.K., Kirby, J.T., 1996. Dynamics of surf-zone turbulence in a spilling breaker. Coast Eng 27, 131-160.
Tomkins, C.D., Adrian, R.J., 2003. Spanwise structure and scale growth in turbulent boundary layers. J Fluid Mech 490, 37-74.
Torrence, C., Compo, G.P., 1998. A Practical Guide to Wavelet Analysis. Bulletin of the American Meteorological Society 79, 61-78.
Tucker, M.J., Pitt, E.G., 2001. Waves in ocean engineering. Elsevier, Amsterdam.
van Rijn, L., Walstra, D., van Ormondt, M., 2007. Unified View of Sediment Transport by Currents and Waves. IV: Application of Morphodynamic Model. Journal of Hydraulic Engineering 133, 776-793.
van Rijn, L.C., 1993. Principles of sediment transport in rivers, estuaries and coastal seas. Aqua Publications, Amsterdam.
van Rijn, L.C., Ribberink, J.S., Werf, J.V.D., Walstra, D.J.R., 2013. Coastal sediment dynamics: recent advances and future research needs. Journal of Hydraulic Research 51, 475-493.
Venditti, J.G., Bennett, S.J., 2000. Spectral analysis of turbulent flow and suspended sediment transport over fixed dunes. Journal of Geophysical Research: Oceans 105, 22035-22047.
Williams, J.J., Metje, N., Coates, L.E., Atkins, P.R., 2007. Sand suspension by vortex pairing. Geophys Res Lett 34, L15603.
Willmarth, W.W., Lu, S.S., 1972. Structure of the Reynolds stress near the wall. J Fluid Mech 55, 65-92.
Wu, F., Jiang, M., 2007. Numerical Investigation of the Role of Turbulent Bursting in Sediment Entrainment. Journal of Hydraulic Engineering 133, 329-334.
Wu, F., Yang, K., 2004. Entrainment Probabilities of Mixed-Size Sediment Incorporating Near-Bed Coherent Flow Structures. Journal of Hydraulic Engineering 130, 1187-1197.
Wyngaard, J.C., Clifford, S.F., 1977. Taylor's Hypothesis and High–Frequency Turbulence Spectra. Journal of the Atmospheric Sciences 34, 922-929.

Yuan, Y., Wei, H., Zhao, L., Cao, Y., 2009. Implications of intermittent turbulent bursts for sediment resuspension in a coastal bottom boundary layer: A field study in the western Yellow Sea, China. Marine Geology 263, 87-96.

Zhou, J., Meinhart, C.D., Balachandar, S., Adrian, R.J., 1997. Formation of coherent hairpin packets in wall turbulence, in: Panton, R.L. (Ed.), Self-sustaining mechanisms of wall turbulence, . Computational Mechanics Publications, Southampton, p. 422p.

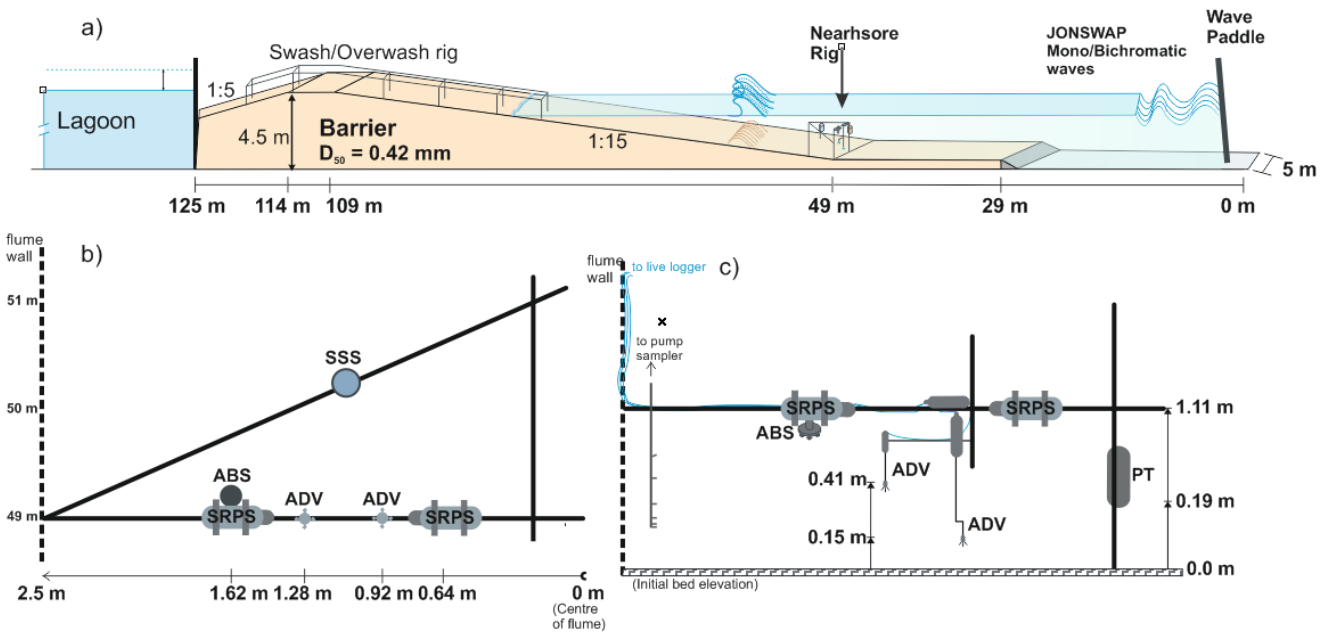

Figure 1. a) Cross-sectional profile of the barrier within the Delta Flume at the start of the BARDEX II experiments, with location of the nearshore instrument frame; b) plan view of instrument rig with distance from the wave paddle on left hand wall, and indicating relative location of instruments from the centre of the flume; c) cross-section view of instrument rig with heights above initial bed elevation. SRPS: sand ripple profiler system; ABS: acoustic backscatter profiler system, ADV: acoustic Doppler velocimetre, SSS: sector scanning sonar, PT: pressure transducer.

Table 1 Wave test conditions, and calculated/measured hydrodynamic properties/parameters

Wave Conditions	Erosive Runs Design characteristics: $\boldsymbol{h = 2.5\,m;\ H_s = 0.8\,m;\ T_p = 8s, JONSWAP}$						Accretive Runs Design characteristics: $\boldsymbol{h = 2.5\,m;\ H_s = 0.6\,m;\ T_p = 12s, JONSWAP}$					
Run (sub-run)	A301-1st	A301-2nd	A301-3rd	A301-4th	mean $\bar{x}$	St. dev. σ_x	A705-	A706	A801-	A802-	mean ($\bar{x}$)	St. dev. σ_x
Water height, $\boldsymbol{h}$ $(\boldsymbol{m})$	2.506	2.512	2.512	2.514	2.51	0.0034	2.507	2.509	2.509	2.509	2.508	0.0008
Measured Significant wave height, $\boldsymbol{H_s}$ (H_{m0}) (m)	0.779	0.761	0.734	0.710	0.750	0.028	0.566	0.705	0.532	0.629	0.608	0.066
Peak wave period, $\boldsymbol{T_p}$ (s)	8.0	8.0	8.98	7.5	8.12	0.53	12.0	12.0	12.0	11.48	12.0	0
Near–bed	0.903	0.	0.99	0.75	0.88	0.08	1.06	1.36	1.36	1.36	1.28	0.12

orbital amplitude, (m) $\mathbf{A_\delta = H_s/(2.\sinh(k.}$		865	8	6		6	5	3	3	3	9	9
Near–bed orbital velocity, $\mathbf{U_{w,orb,\delta} = A_\delta.\omega}$ (m/s) (Van Rijn, 1993)	0.709	0.679	0.698	0.634	0.680	0.029	0.557	0.713	0.713	0.713	0.674	0.068
Wave Reynolds number, $\mathbf{Re_{w,\delta}}$ (Soulsby and Clarke, 2005a)	2.53E+05	2.53E+05	2.38E+05	2.38E+05	2.45E+05	0.7E+05	2.14E+05	2.26E+05	2.40E+05	2.37E+05	2.29E+05	0.1E+05
Wave boundary layer thickness, δ_w (m), calculated from measured stress	0.249	0.140	0.128	0.123	0.160	0.052	0.177	0.184	0.178	0.194	0.183	0.007
Wave friction factor, f_w using TKE method (Thompson et al., 2012)	0.020	0.032	0.026	0.023	0.025	0.004	0.024	0.024	0.024	0.023	0.024	0.0

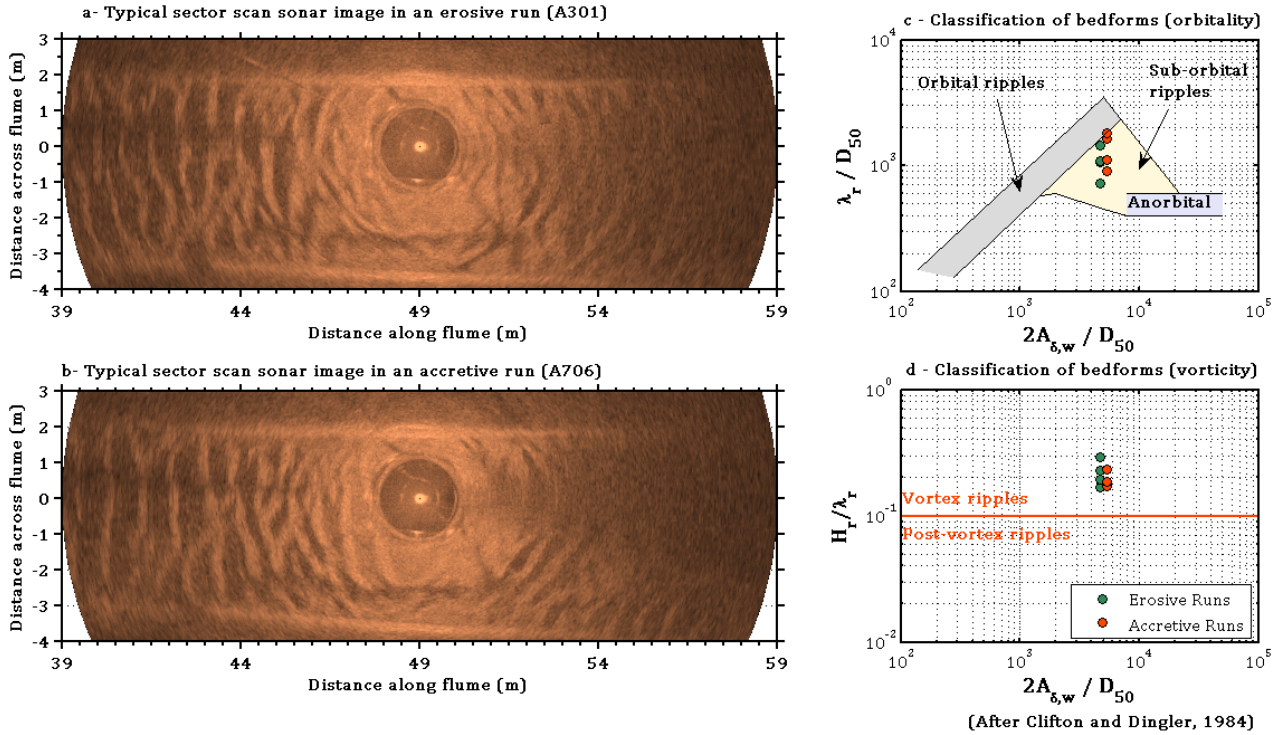

Figure 2. Typical 2D ripple configurations observed via backscatter intensity along and across the flume in the vicinity of the instrumented offshore frame, for a) erosive, and b) accretive wave runs. Classification of bedform in terms of c) orbitality, and d) vorticity for the average bedform characteristic lengths is after Clifton and Dingler, (1984).

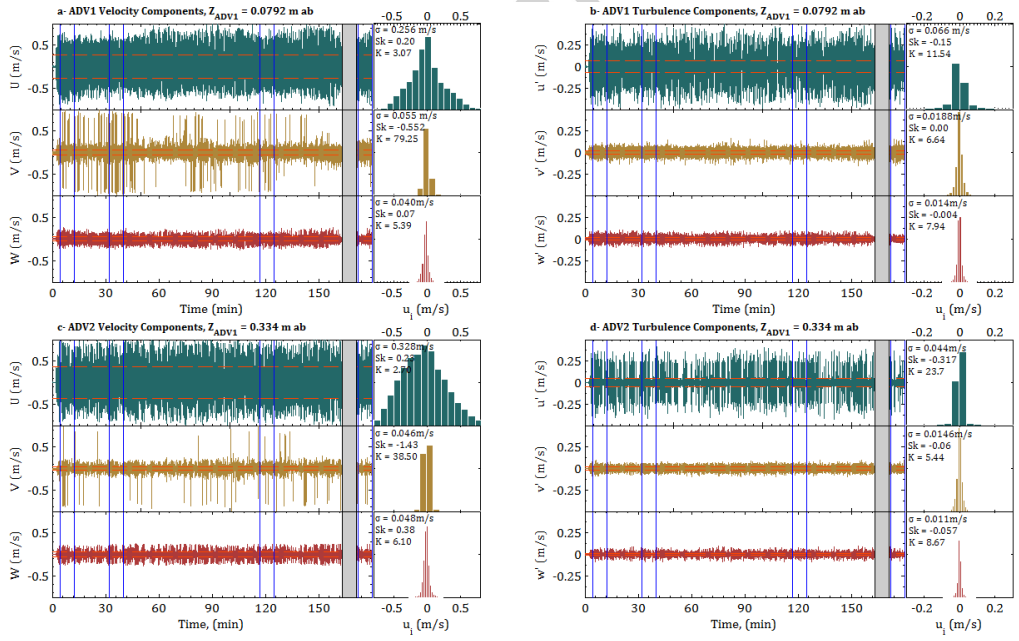

Figure 3. Time series and probability density functions of 3D velocity (U, V, and W) and inherent turbulence (u', v', w') components, in the streamwise/along-flume (dark green), crosswise (gold), and vertical (orange) for the entire experimental wave run A301 (Hs = 0.8m, Tp = 8 s). The horizontal

dashed lines (red) in the time series represent ± 1 standard deviations; while the vertical blue lines delimit the 4 sub-records analysed; σ is standard deviation, Sk is skewness , and K is Kurtosis.

Table 2. Statistical properties of the three turbulence components measured within (ADV1) and outside (ADV2) the wave boundary layer for the two types of wave conditions. These are averages of the 4 sub-sampled records analysed for each of the erosive and accretive runs.

Wave run - subrecord	ADV	Height above bed (m)	turbulence component	Standard deviation	Variance	Skewness	Kurtosis
Erosive Runs	ADV 1	0.0792	u'	0.27±0.027	0.07±0.014	0.27±0.06	2.97±0.38
			v'	0.05±0.005	0.00	-0.78±1.3	37.47±28.76
			w'	0.04±0.005	0.00	0.09±0.38	6.52±1.68
	ADV 2	0.334	u'	0.33±0.015	0.11±0.01	0.26±0.08	2.61±0.07
			v'	0.09±0.004	0.00	-1.70±1.10	39.22±27.08
			w'	0.05±0.002	0.00	0.34±0.22	5.99±0.59
Erosive Runs	ADV 1	0.09±00.1	u'	0.25±0.025	0.06±0.012	0.32±0.12	3.04±0.0.33
			v'	0.06±0.013	0.00	1.10±1.32	36.69±23.43
			w'	0.03±0.003	0.00	-0.18+0.54	7.94±2.03
	ADV 2	0.337±0.016	u'	0.28±0.015	0.08±0.009	0.37±0.039	3.08±0.2
			v'	0.04±0.003	0.00	-0.60±0.72	22.75±22.28
			w'	0.04±0.002	0.00	0.01±0.12	7.30±1.04

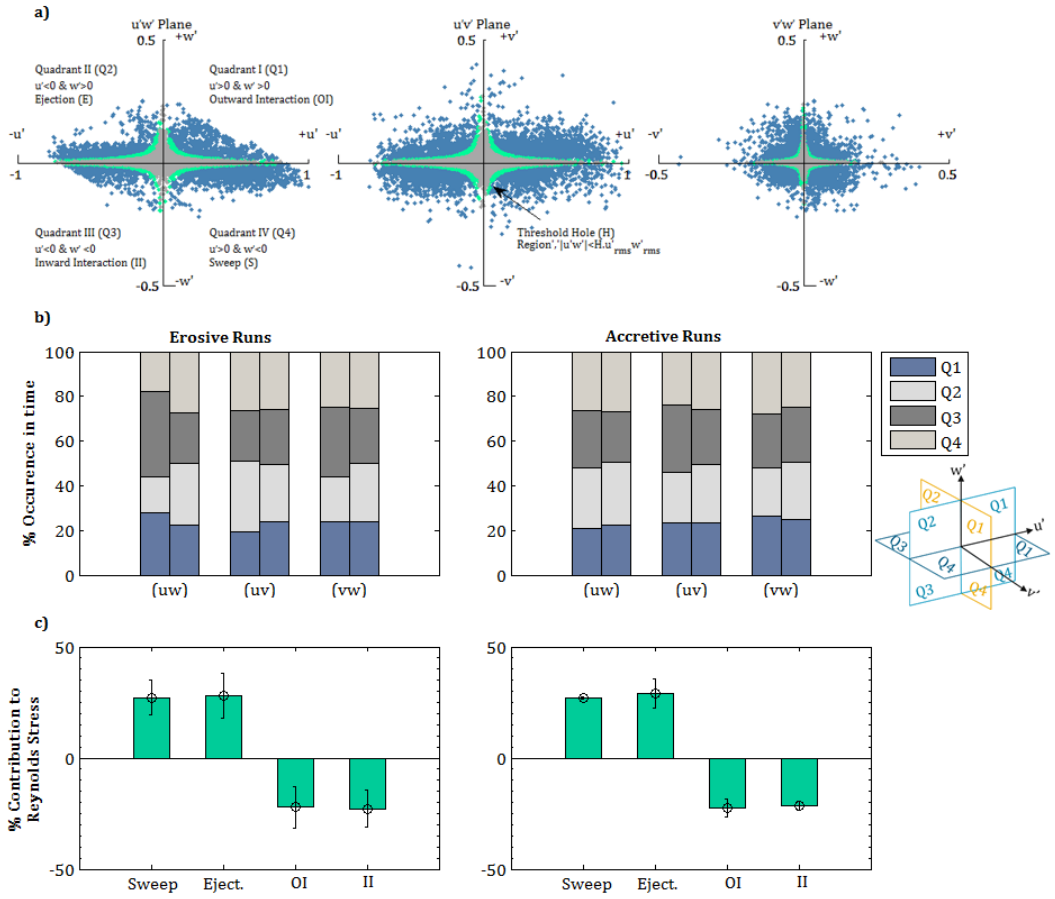

Figure 4 a) Quadrant analyses of instantaneous Reynolds' stresses in three planes for an example 8 minute sub-record from wave series A3-01(Erosive). Areas delimited by hole sizes defined by H= 1 (gray) and H=2 (green) are highlighted. b) average percentage of occurrence in time occupied by the 4 Quadrant-type events in each plane, in the erosive and accretive runs, before and after filtering the periodic signal, with H =0; and (c) average contribution to Reynolds' stress by the 4 types of motion in (u'w').

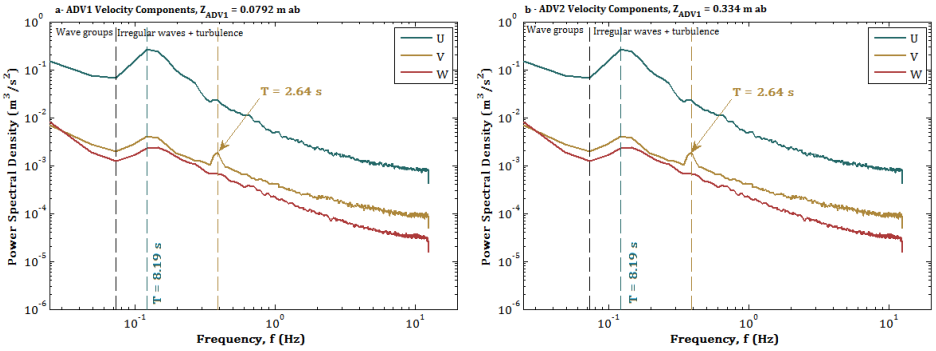

Figure 5. Time series and spectral analysis of 3D fluctuating velocity components, in the streamwise/along-flume (dark green), crosswise (gold), and vertical (orange) for the entire experimental wave run A301 (Hs = 0.8m, Tp = 8 s) measured (a) within; and (b) outside the oscillatory benthic boundary layer, δ_w. Power spectral densities calculated using Welch's method with a Hann window (2^11 length) with 50% overlap, sampling frequency 25 Hz). Peak wave frequencies are indicated.

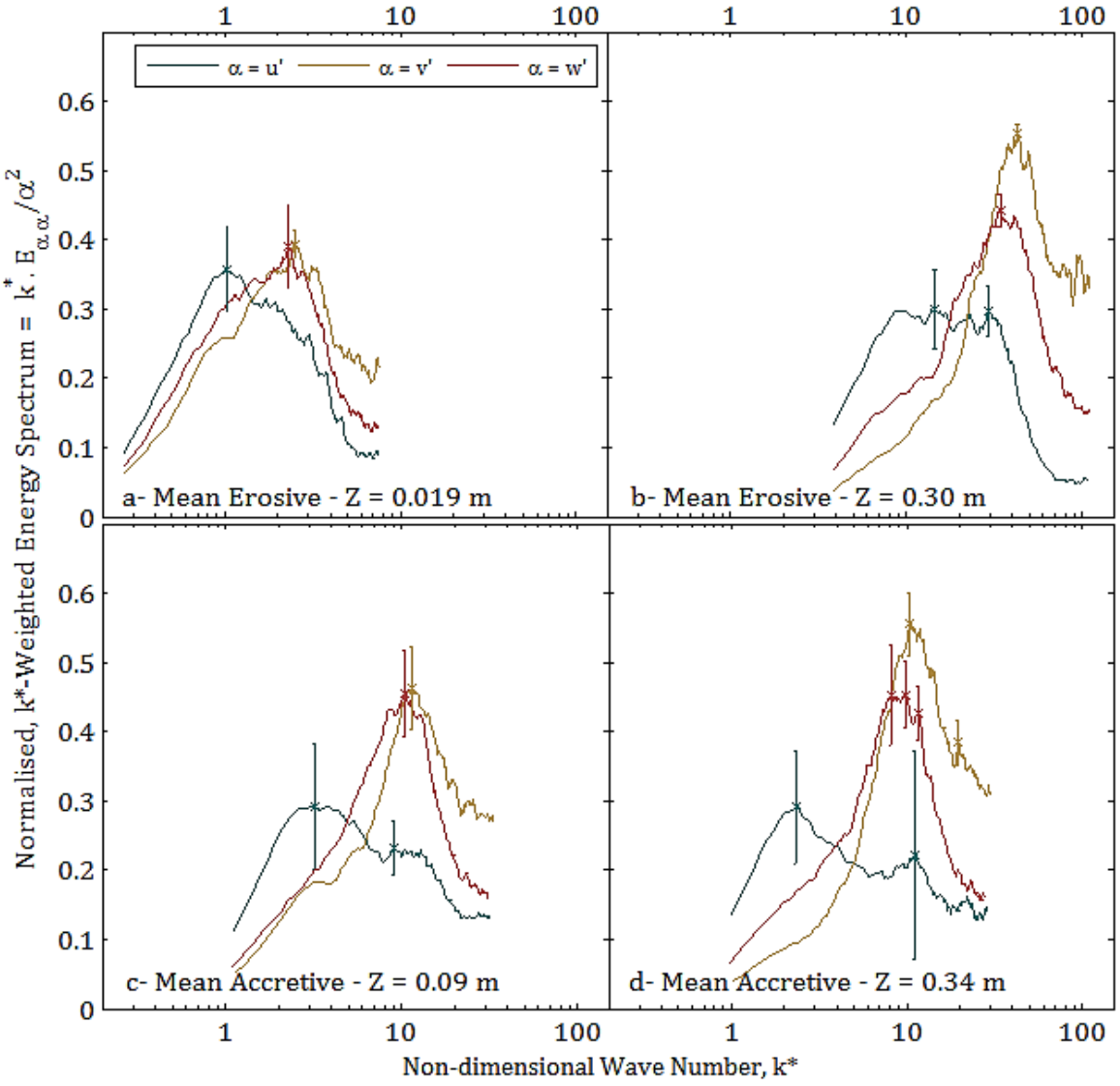

Figure 6. Average normalised non-dimensional wavenumber (K*)-weighted turbulent energy spectra of the three turbulence components, (u', dark green), crosswise (v', gold), and vertical (w', orange) turbulence components; measured within the benthic bounary layer (a, and c) and outside the wave boundary (b, and e), for the erosive and accretive wave runs, respectively.

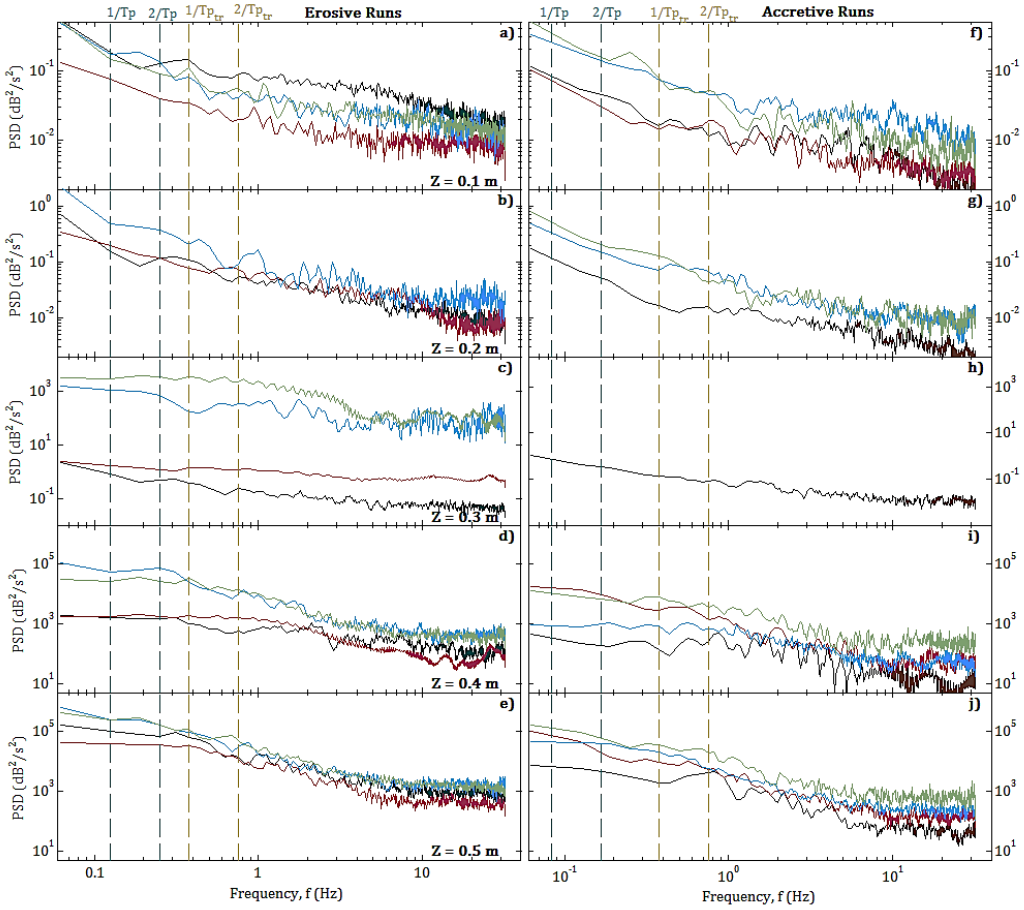

Figure 7. Power spectral densities (PSD) of the suspended sediment backscatter at 5 different elevations above the bed, for all the analysed erosive (left panel), and accretive (right panel) wave runs. The first (1/Tp) and second (2/Tp) harmonics of the progressive wave forcing, and the transverse standing waves are shown by the green and golden dashed lines, respectively.

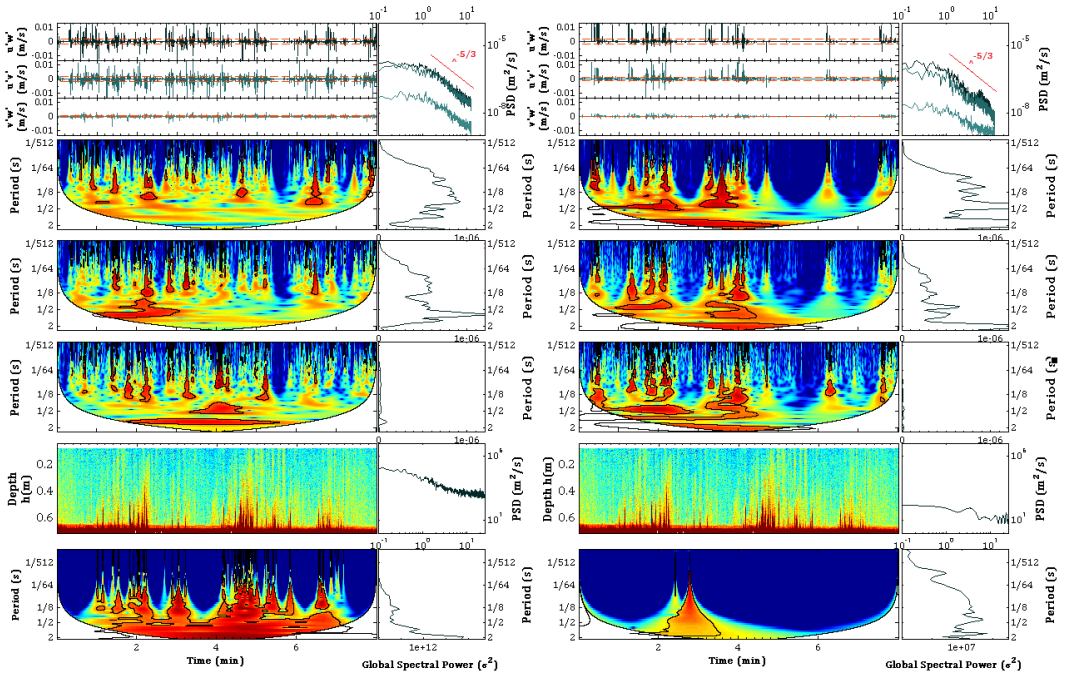

Figure 8. Time-frequency properties of the three instantaneous Reynolds stresses (u'w', u'v', and v'w') and suspended sediment concetrations, measured within(left handside), and outside (right handside) the benthic wave boudnary layer. In each panel, the top three subplots show the time series of the three aforementioned stresses, respectively, together with their frequency spectrum (through a Fourier transform) in which universal Kolmogorov-Obukhov rate of inertial dissipation (^-5/3) is represented by the red line. The following three sub-panels present the time-series of continuous wavelet transforms (CWT) for each of the stresses in the time-frequency domain, presented in the same order, together with their global spectral power (integrated variance) across the various frequency scales (inverse period). Subsequently, the lower two sub-panels show the time series of vertical suspension (logarithmic backscatter, higher values in warmer colours) profiles below the ABS sensor head, the power spectral densities of suspended sediment concentration at the level of the corresponding ADV (ADV1 on the left, ADV2 on the right), and the related continuous wavelet transform of the suspension time series at that elevation, together with its global spectral power. In the time-frequency domains, warmer colours indicate higher power (variance), the white-shaded region represents the cone of influence where edge effects may distort the image, and the thick contours represent the 95% confidence limit (5% significance against red noise).

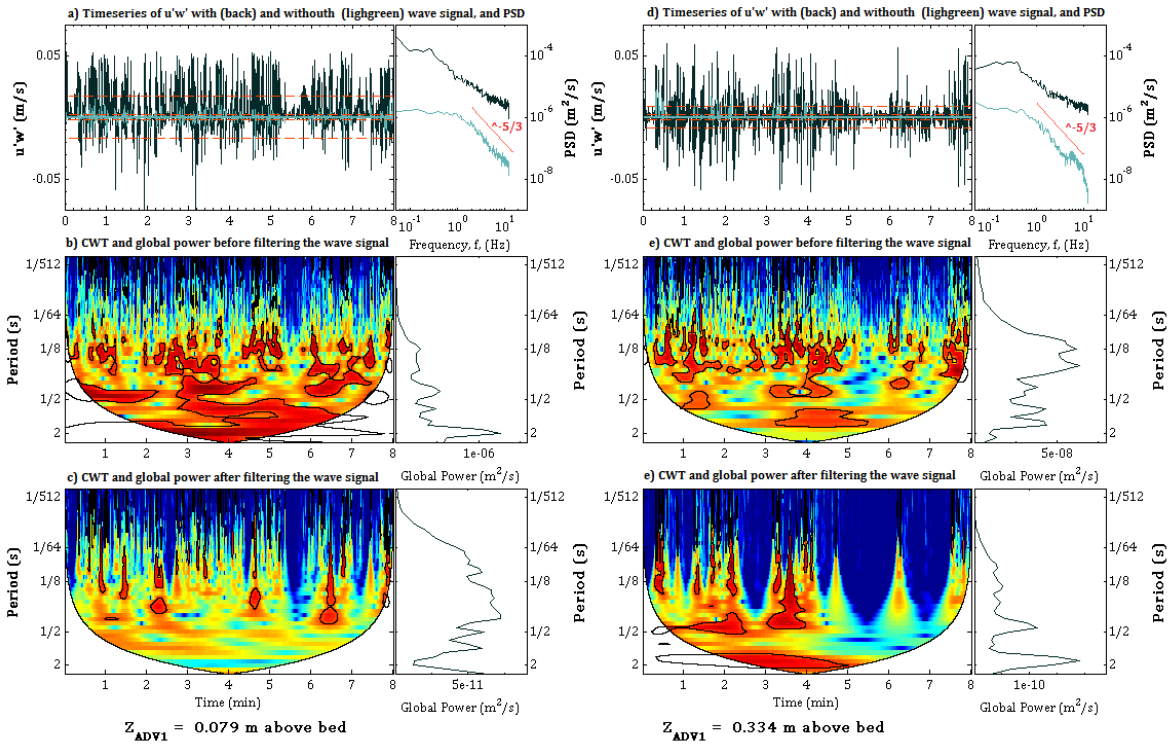

Figure 9. Influence of wave-signal on the time-frequency properties of Reynolds stress in the streamwise-vertical plane (u'w'), measured near the bed (left panel), and putside the wave boundary layer (right panel). In each panel, top sub-plots (a, and d) show the time series of Reynolds stress (before and after filtering out the wave signal), together with its corresponding frequency spectrum (by Fourier transform). The dashed horizontal lines indicate $\pm 1.\sigma$ (standard deviation). The rate of inertial dissipation is shown by the sloping red line in the frequency plot. The middle (b and e) and bottom (c and d) sub-panels sow the time-series of continuous wavelet transform (CWT) of the Reynolds stress before and after filtering out the wave signal, respectively, together with the corresponding global power spectrum. In the time-frequency domains, warmer colours indicate higher power (variance), the white-shaded region represents the cone of influence where edge effects may distort the image, and the thick contours represent the 95% confidence limit (5% significance against red noise).

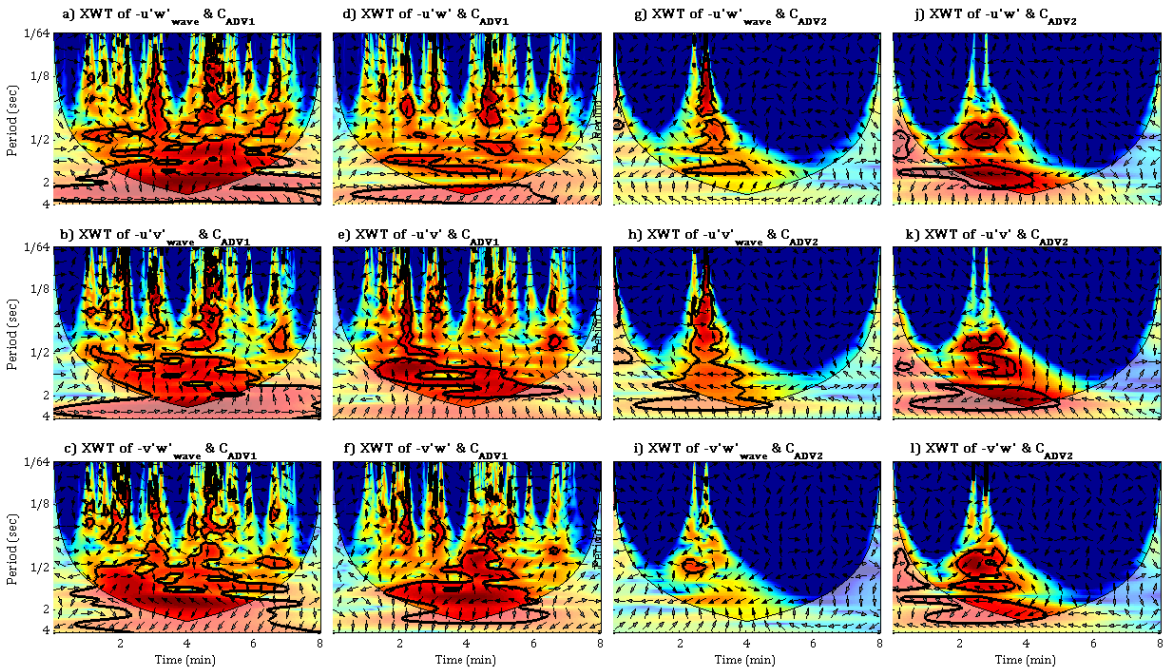

Figure 10. Cross wavelet transforms of instantaneous 3 dimensional Reynolds Stresses and (downsampled) Sediment Concentrations within (ADV1) and outside (ADV2) the bottom wave boundary layer during erosive wave run A3-01 (2nd), before and after fitlering out the periodic signal from the turbulent component. The light-shaded region represents the cone of influence where edge effects may distort the image. The thick contours represent the 95% confidence limit (5% significance against red noise). The relative phase is shown in arrows (with righ arrow indicating inphase, left arrows indicating anti-phase, and vertical arrows indicate Reynolds stresses leading by 90 degrees.